ON THE MECHANICS OF THE HYDROGEN INTERACTION WITH SINGLE CRYSTAL PLASTICITY

BY

GREGORY J. SCHEBLER

THESIS

Submitted in partial fulfillment of the requirements
for the degree of Master of Science in Theoretical and Applied Mechanics
in the Graduate College of the
University of Illinois at Urbana-Champaign, 2010

Urbana, Illinois

Adviser:

Professor Petros Sofronis

Abstract

This thesis presents a model to simulate the effects of hydrogen on the mechanical behavior of single crystals. A macroscopic crystal plasticity model is formulated based on the fundamentals of the hydrogen-dislocation interactions. Various hardening evolution equations are investigated and employed in a physically-based model. The presence of hydrogen is incorporated into the constitutive relations through basic equations to simulate its effects on dislocation activation, multiplication, and annihilation. The crystal plasticity model is then implemented in a computationally realizable solution to the single crystal uniaxial tension problem.

The present model is designed within a crystal plasticity framework for an FCC single crystal. Features that incorporate the hydrogen effect into the constitutive model have been designed to directly capture observed effects in single crystals. Experimental data available in uniaxial tension for single crystal nickel specimens are used to calibrate the model. The sensitivities of the model are investigated through varying the magnitudes of the parameters controlling the mechanical behavior and how it is influenced by the presence of hydrogen. Through this study, a constitutive theory on how hydrogen affects the deformation is proposed and areas of further research are discussed.

Acknowledgements

A great deal of thanks is due to Professor Petros Sofronis for giving me the opportunity to work on this project, for providing me with all of the resources needed to complete a successful work, and most importantly, for the hours he spent working with me on this research. My thanks also go to Dr. Mohsen Dadfarnia for much of the guidance and direction for this project. I would also like to thank Professor Nikolaos Aravas for his helpful insight and support throughout the duration of my research. This study was supported financially by Los Alamos National Laboratory under grant LANL 62568-001-08 to the University of Illinois.

Table of Contents

1. Introduction

It has been well established that hydrogen has a detrimental effect on almost all structural materials (Hirth, 1980; Birnbaum and Sofronis, 1994; Birnbaum et al., 1997). In particular, materials in the presence of hydrogen are observed to fail at load levels far lower than those found in comparable tests performed in the absence of hydrogen. This effect is typically known as "hydrogen embrittlement" and is characterized by a loss of macroscopic ductility, a reduction of tensile strength or fracture toughness, a change in fracture mode, etc. (Hirth, 1980). One of the mechanisms responsible for this observed effect is hydrogen enhanced local plasticity (HELP) (Beachem, 1972; Birnbaum and Sofronis, 1994; Robertson, 2001). Evidence in support of this mechanism comes from both experimental observations (Sirois and Birnbaum, 1992; Robertson, 2001) and theoretical calculations (Sofronis and Birnbaum, 1995), from which it has been shown that the presence of hydrogen in solid solution decreases the barriers to dislocation motion, thereby increasing the amount of deformation that occurs in a localized region adjacent to the fracture surface.

This work seeks to model the effects of the presence of hydrogen in structural materials by accounting for hydrogen solute interactions with the material microstructure subject to deformation. A three dimensional constitutive model is explored and developed to incorporate the effects of hydrogen. The constitutive model is then implemented computationally for single crystal face-centered cubic (FCC) metals and used in uniaxial tension simulations. This investigation is motivated by the expectation that a successful description of the hydrogen-dislocation interactions in single crystals can eventually lead to a predictive model for macroscopic polycrystalline metals. Certainly, in creating a physically-based constitutive model, the underlying mechanisms of these interactions must be thoughtfully considered. Lastly, the computationally-implemented constitutive model can be applied to carry out calculations for various boundary value problems, such as a crack tip in a single crystal.

2. Literature Review

In this section, the body of work pertaining to the mechanical behavior of single crystals and the effect of hydrogen on this behavior is reviewed. In particular, experimental studies that capture the distinct stages of hardening in single crystals under tensile loading are explored. Also, special attention is given to constitutive models in which the dislocation density is the primary state variable due to its pertinence to the hydrogen problem.

2.1. Hardening Models for Single Crystals

Many studies have been performed on the mechanical behavior of FCC crystals, and special care has been given to address the varying stages of the stress-strain response for these crystals. In this work, it is aimed that the hardening model adequately captures effects of both stage I and stage II hardening. Detailed descriptions of the stages of work hardening have been given by Kocks and Mecking (2003). Stage I hardening is observed in tensile single crystal specimens when the axis of loading is chosen such that only one slip system is initially active. This type of deformation in which a single slip system (termed the "primary" system) is active is often denoted as easy glide and is characterized by a very low hardening rate. Stage I hardening terminates with the onset of a steep and almost linear branch which is denoted stage II. This stage corresponds to the activation of additional slip systems, which occurs when the resolved shear stresses on those slip systems reach their critical values as the applied stress is increased.

Stage II hardening depends strongly on the interactions between dislocations from multiple slip systems. Therefore, it is important to consider how the effect of dislocation-dislocation interactions is incorporated into the constitutive model to capture the increased hardening observed during stage II. For symmetrical tensile axis orientations (for example, the [001] and [111] directions), stage I is not observed at all since multiple slip systems become active at the onset of plastic deformation. The stage II hardening is observed to be highest in orientations nearest to the symmetrical orientations in which stage I is either short or absent (Kocks and Mecking, 2003).

A crucial component of the constitutive relations is the evolution of the critical resolved shear stress for slip system α, τ_{cr}^{α} (in this work, Greek indices are used to reference slip systems). A general relation was given by Hill (1966) in terms of the plastic shear strains on each slip system, which are denoted by γ^{α}. In Hill's formulation, the plastic strains are defined such that the lattice geometry is not disturbed, and $\gamma > 0$ on active slip systems, while $\gamma = 0$ for the remaining slip systems. The evolution of τ_{cr}^{α} is given as follows:

$$\dot{\tau}_{cr}^{\alpha} = \sum_{\beta=1}^{n} h_{\alpha\beta}\dot{\gamma}^{\beta}, \tag{1}$$

where the components $h_{\alpha\beta}$ are the instantaneous hardening moduli, n is the number of slip systems, and a superposed dot denotes time differentiation. A detailed description of the characterization of the instantaneous hardening moduli was done by Bassani and Wu (1991) for a copper single crystal. The first index in the hardening moduli, α, corresponds to the critical resolved shear stress as it is calculated in Eq. (1), and the second index, β, corresponds to the shear strain on slip system β. Therefore, when the two indices are equal, the modulus is associated with the self-hardening of a material, and when the two indices are not equal, the modulus corresponds to the latent hardening. However, it was noted by Bassani and Wu (1991) that choosing the latent hardening values to be zero still allows excellent agreement with experimental observations, so these values are generally chosen to be zero. This simplification reduces $[h_{\alpha\beta}]$ to a diagonal matrix that will be positive definite if all of the components remain positive. The positive definiteness of the matrix is a necessary condition so that all of the strain rates can be uniquely determined for the case of load-controlled deformation.

To couple the hardening response with the hydrogen effect, the dislocation density is used as the governing physical variable of the strain hardening phenomenon. The relationship between the critical resolved shear stress, τ_{cr}, and the dislocation density, ρ, is given as (Taylor, 1934)

$$\tau_{cr} = \alpha'\mu b\sqrt{\rho}, \tag{2}$$

where α' is a proportionality constant, μ is the shear modulus, and b is the magnitude of the dislocation Burgers vector. The generalization of Eq. (2) to all slip systems is given by (e.g., Tabourot et al., 1997)

$$\tau_{cr}^{\alpha} = \mu b \sqrt{\sum_{\beta=1}^{n} a_{\alpha\beta} \rho^{\beta}} \,, \tag{3}$$

where $[a_{\alpha\beta}]$ is the interaction matrix, which measures the effect of the dislocation density on slip system β, ρ^{β}, on the critical resolved shear stress on slip system α, τ_{cr}^{α}.

To create a constitutive model that can incorporate hydrogen, an evolution equation for the dislocation density on a given slip system is considered. For continuum models utilizing the bulk dislocation density, the following classical evolution equation is applied (Estrin and Mecking, 1984):

$$\dot{\rho} = (c_1 \sqrt{\rho} - c_2 \rho)\dot{\gamma} \,, \tag{4}$$

where c_1 and c_2 are material constants related to dislocation multiplication and recovery processes, respectively, and γ is shear strain. The generalization of Eq. (4) is described by Tabourot et al. (1997) in terms of the dislocation densities on each individual slip system as

$$\dot{\rho}^{\alpha} = \frac{1}{b} \left(\frac{\sqrt{\sum_{\beta=1}^{n} a'_{\alpha\beta} \rho^{\beta}}}{K} - 2 y_c \rho^{\alpha} \right) \dot{\gamma}^{\alpha} \,, \tag{5}$$

where K is a material parameter, y_c is the mean distance between two dislocations, and the matrix $[a'_{\alpha\beta}]$ is the interaction matrix that describes the effect of the forest dislocations in slip system β on the mean free path of dislocations in slip system α.

More recently, a hardening model was proposed for FCC single crystals to adequately capture hardening effects in single crystal under uniaxial tension (Kubin et al., 2008; Devincre et al., 2008). In this model, the evolution equation for the dislocation density on slip system α takes the form

$$\frac{d\rho^{\alpha}}{d\gamma^{\alpha}} = \frac{1}{b} \left(\frac{1}{L^{\alpha}} - y \rho^{\alpha} \right) \tag{6}$$

where L^{α} is the dislocation mean free path. In particular, for cases in which the loading axis lies along symmetrical orientations such as $[211]$, $[111]$, or $[001]$ in which four, three, and two slip systems are initially active, respectively, the mean free path can be expressed as

$$\frac{1}{L^{\alpha}} = \frac{\tau_{cr}^{\alpha}}{\mu b K_{hkl}}, \tag{7}$$

where K_{hkl} are orientation dependent coefficients. It is particularly interesting to note that the substitution of Eq. (7) into Eq. (6) yields a dislocation density evolution equation that matches the general form of Eq. (5) under the condition that the interaction matrices $[a_{\alpha\beta}]$ and $[a'_{\alpha\beta}]$ are identical.

In the model of Bassani and Wu (1991), the constitutive equations were constructed in order to characterize the multislip behavior of single crystals. The model takes the form of Eq. (1) in which the coefficients $h_{\alpha\beta}$ are a multiplicative combination of functions governing single slip and slip interactions as follows:

$$h^{\alpha\beta} = \begin{cases} F(\gamma^{\alpha}) G(\{\gamma^{\delta}, \delta = 1,2,...,N, \delta \neq \alpha\}), & \alpha = \beta \\ q h^{\alpha\alpha}, & \alpha \neq \beta \end{cases} \tag{8}$$

with

$$F(\gamma^{\alpha}) = (h_0 - h_s)\,\mathrm{sech}\left[\frac{(h_0 - h_s)\gamma^{\alpha}}{\tau_I - \tau_0}\right] + h_s \tag{9}$$

and

$$G(\{\gamma^{\delta}, \delta = 1,...,N, \delta \neq \alpha\}) = 1 + \sum_{\substack{\delta=1 \\ \delta \neq \alpha}}^{n} f_{\alpha\delta} \tanh(\gamma^{\delta} / \gamma_0). \tag{10}$$

It is necessary to consider the physical significance of the constants applied in the above relations as given by the designers: τ_0 is the initial critical resolved shear stress, τ_I is the "stage I stress" at which large plastic flow initiates, h_0 is the hardening modulus after initial yielding, h_s is the hardening modulus during stage I, or easy glide, γ_0 is the shear strain at which the interaction between slip system α and β reaches peak strength, and

n is the number of active slip systems. The matrix $[f_{\alpha\beta}]$ contains the magnitudes of the strength of slip interactions between slip system α and β.

The form of the function F was chosen by Bassani and Wu (1991) to be consistent with observations of active hardening at small plastic strains while giving finite or zero hardening at large γ^{α}. The form of the function G was chosen to equal unity when its arguments are all zero since there are no slip interactions when there is no slip on other systems. Also, for very large values of γ^{β} ($\beta \neq \alpha$), the function G approaches a finite value.

2.2. Effects of Hydrogen on Single Crystal Plasticity

Many engineering applications that motivate understanding of the effect of hydrogen on mechanical behavior involve polycrystalline metals. Prior to the development of a comprehensive polycrystalline model, a thorough description of the hydrogen-dislocation interactions within single crystals can be constructed to obtain a physically-based model for a general class of engineering materials. Experimental investigations into the effect of hydrogen in a single crystal material have provided insight into a unique behavior that is not immediately reflected in similar studies on polycrystalline metals. These experiments offer valuable insight into the mechanisms that should be the basis for a constitutive model incorporating the hydrogen-dislocation interactions. Research performed on polycrystalline metals is also applicable to the present study when individual mechanisms are analyzed rather than the bulk behavior of the material.

A major incentive to study single crystals is found by way of the contradictory results that have often been obtained in regards to the effect hydrogen has on yielding and flow stresses in macroscopic tensile tests of polycrystalline metals. Experimental measurements that have been obtained on tension specimens in the presence of hydrogen support both increasing (Ulmer and Altstetter, 1991; Abraham and Altstetter, 1995) and decreasing (Kimura and Birnbaum, 1987; Matsui et al., 1979a, 1979b; Moriya et al. 1979) yield and flow stresses. Through experimentation and modeling of single crystals, it is expected that a more fundamental understanding of how hydrogen impacts yield and flow stresses can be reached.

A key mechanism at the root of the effect of hydrogen on the mechanical behavior of single crystals is the hydrogen interactions with dislocations. Studies on polycrystalline nickel have shown that the presence of hydrogen increases the mobility of dislocations (Robertson and Birnbaum, 1986; Robertson, 2001). These observations suggest that lower applied stresses are required to move dislocations in the presence of hydrogen compared to the absence of hydrogen. Observations have shown increased velocities due to hydrogen for isolated dislocations, dislocations intersected by forest dislocations, and dislocations of different character (screw, edge, etc.) (Robertson, 2001). These general observations would seem to suggest that reduced hardening may be found in the deformation of a single crystal in both stage I, where dislocations move within a single active slip plane, and stage II, in which dislocations interact with forest dislocations in other slip planes. The results of Robertson and Birnbaum (1986) also suggest that the dislocation generation rate is increased by the presence of hydrogen, though the work of Ulmer and Altstetter (1991) suggests that the generation of dislocations is initially blocked by the presence of hydrogen.

The effect of hydrogen on the initial activation of dislocations is associated with the macroscopic yield stress in single crystals subject to uniaxial tension. Experimental measurements of polycrystalline FCC metals have pointed to an elevated yield stress resulting from hydrogen-charging in 304 (Ulmer and Altstetter, 1991) and 310s (Abraham and Altstetter, 1995) stainless steels. In these works, the observed elevation has been attributed to the hydrogen atmosphere locking of Frank-Read and other dislocation sources, which can certainly be the mechanism that is active in single crystals as well.

Of significant interest to the present study are the experimental results for uniaxial tension tests of single crystal FCC specimens. Though only a limited number of investigations have been performed on such specimens, these investigations provides valuable insight into the effect of hydrogen-charging on single crystal tensile specimens. In particular, the works of Yagodzinskyy and coworkers (2003, 2009) and Delafosse and coworkers (2009) are considered. The experiments conducted in these bodies of work were performed on single crystal specimens oriented for easy glide; however, the tests performed by Delafosse et al. were done at a much higher strain rate (10^{-2} s^{-1}) that those

performed by Yagodzinskyy et al., where the strain rate used was near 10^{-4} s^{-1} for both tests.

From these tests, there are several significant observations in relation to the effects of hydrogen on tensile behavior of FCC single crystals; these observations are summarized as follows:

- An increase in uniaxial tension yield strength of about 20-25% in pure nickel single crystal tensile specimens (Delafosse et al., 2009; Yagodzinskyy et al., 2009) and about 30% in austenitic stainless steel single crystals (Yagodzinskyy et al., 2003).
- The stress-strain curve for the hydrogen-charged single crystal in tension exhibits a prolonged stage I, i.e. hydrogen delays the emergence of stage II.
- A significant increase in the work hardening is observed during stage II (Delafosse et al., 2009).

In this work, the simulation of the uniaxial tension response of single crystals will be done quasi-statically, so more attention is given to the experimental results corresponding to low strain rate tests. Experimental results for the high strain rate tests are still considered, though strict agreement between these results and the model is not enforced.

Despite the different strain rates used in these experiments, both exhibited elevated yield stresses at the onset of plastic deformation. Indeed, it seems consistent for the FCC metals studied that yield stress can be expected to increase by 20-30% when the material is charged with hydrogen. Observations of a prolonged stage I are also of great interest as such results indicate an increase in plastic strain along specific slip systems in the single crystal prior to stage II and the accompanying macroscopic hardening.

3. Formulation

The formulation of the constitutive equations has been performed using finite deformation crystal plasticity while incorporating the dilatational effect of lattice hydrogen and the effect of trapped hydrogen on the dislocation behavior. The constitutive equations are then used to solve the uniaxial tension boundary value problem. Due to the duration of the problem being solved, the hydrogen concentration is assumed fixed at any material point within the specimen, and hence the dilatational effect will vanish. The numerical integration of the constitutive equations introduced in this section is provided in Appendix A.

3.1. Large Strain Deformation in the Presence of Hydrogen

To describe the finite deformation elastoplastic response of the material, a multiplicative decomposition of the deformation gradient is employed (Lee, 1969). To include the dilatational effect from the presence of hydrogen, an additional term is introduced such that the total deformation gradient is expressed as

$$\mathbf{F} = \mathbf{F}^e \cdot \mathbf{F}^h \cdot \mathbf{F}^p , \tag{11}$$

where $\mathbf{F}^e$, $\mathbf{F}^h$, and $\mathbf{F}^p$ are elastic, hydrogen, and plastic parts of the deformation gradient, respectively. A schematic representation of this decomposition is provided in Fig. 1.

The velocity gradient is given in terms of the deformation gradient as

$$\mathbf{L} = \dot{\mathbf{F}} \cdot \mathbf{F}^{-1} \tag{12}$$

and can be expressed in terms of the individual parts of the deformation gradient by using (11):

$$\mathbf{L} = \dot{\mathbf{F}}^e \cdot \mathbf{F}^{e-1} + \mathbf{F}^e \cdot \dot{\mathbf{F}}^h \cdot \mathbf{F}^{h-1} \cdot \mathbf{F}^{e-1} + \mathbf{F}^e \cdot \mathbf{F}^h \cdot \dot{\mathbf{F}}^p \cdot \mathbf{F}^{p-1} \cdot \mathbf{F}^{h-1} \cdot \mathbf{F}^{e-1} . \tag{13}$$

The deformation due to hydrogen is purely dilatational (Peisl, 1978), thus the hydrogen part of the deformation gradient is expressed as (Sofronis, 1995)

$$\mathbf{F}^h = \left(1 + \frac{e^h}{3}\right)\mathbf{I} , \tag{14}$$

where $e^h = (c - c_0)\lambda$, c and c_0 are total current and initial (stress-free) concentrations of hydrogen at the material point (expressed in hydrogen atoms per lattice atom), respectively, $\lambda = \Delta v / \Omega$, Δv is the volume change per atom of hydrogen introduced into solution and is related to the partial molar volume of hydrogen $V_h = \Delta v N_A$ in solution, N_A is Avogadro's number, Ω is the mean atomic volume of the host metal atom, and $\mathbf{I}$ is the second-order identity tensor. From Eq. (14), one readily finds

$$\begin{aligned} \dot{\mathbf{F}}^h \cdot \mathbf{F}^{h-1} &= \tfrac{d}{dt}\left(1 + \frac{(c - c_0)\lambda}{3}\right)\mathbf{I} \cdot \left(1 + \frac{(c - c_0)\lambda}{3}\right)^{-1}\mathbf{I} \\ &= -\frac{\dot{c}\lambda}{3\left(1 + \frac{(c - c_0)\lambda}{3}\right)}\mathbf{I} = \frac{\dot{c}\lambda}{3 + (c - c_0)\lambda}\mathbf{I} = \frac{1}{3}\Lambda(c)\dot{c}\mathbf{I}, \end{aligned} \tag{15}$$

where $\Lambda(c) = \lambda / [1 + \lambda(c - c_0)/3]$. Then, Eq. (13) becomes

$$\mathbf{L} = \mathbf{L}^e + \mathbf{L}^h + \mathbf{L}^p \tag{16}$$

with

$$\mathbf{L}^e = \dot{\mathbf{F}}^e \cdot \mathbf{F}^{e-1}, \tag{17}$$

$$\mathbf{L}^h = \frac{1}{3}\Lambda(c)\dot{c}\mathbf{I}, \tag{18}$$

$$\mathbf{L}^p = \mathbf{F}^e \cdot \mathbf{L}_i^p \cdot \mathbf{F}^{e-1}, \tag{19}$$

and

$$\mathbf{L}_i^p = \dot{\mathbf{F}}^p \cdot \mathbf{F}^{p-1}. \tag{20}$$

Note that $\mathbf{L}^e$ is the elastic part of the velocity gradient, $\mathbf{L}_i^p$, which is defined in the intermediate configuration (Aravas, 1994), is the velocity gradient due to slip, and $\mathbf{L}^h$ is the hydrogen part of the velocity gradient. The intermediate configuration may be defined as the "undeformed" configuration for the elastic part of the deformation, or the "deformed" configuration for the plastic part of the deformation. The hydrogen part of the deformation can be ignored for the present discussion since its dilatational effect will not affect the lattice orientation. The usefulness of defining $\mathbf{L}_i^p$ in the intermediate configuration can be seen in Fig. 1; the definition of slip system α in the intermediate configuration is identical to the definition in the original configuration, in which the slip plane normal and slip direction are fixed and easily identifiable.

The component of the velocity gradient for the plastic deformation plasticity is expressed in the intermediate configuration (Aravas, 1991) as

$$\mathbf{L}_i^p = \sum_\delta \dot{\gamma}^\delta \mathbf{s}_0^\delta \mathbf{m}_0^\delta , \tag{21}$$

where $\dot{\gamma}^\delta$ is the rate of simple shearing on slip system δ and $\mathbf{s}_0^\delta$ and $\mathbf{m}_0^\delta$ are the slip direction and slip normal (in the intermediate configuration) on the slip system δ, respectively. The summation is carried out over all slip systems. The slip direction vector transforms with the lattice deformation from the intermediate configuration to the current configuration, as seen in Fig. 1; it can be written in the current configuration as

$$\mathbf{s}^\delta = \mathbf{F}^e \cdot \mathbf{s}_0^\delta . \tag{22}$$

The slip normal vector, $\mathbf{m}_0^\delta$, remains normal to the slip plane during the deformation. The area transformation of an element dS_0 on this plane is given by Nanson's formula as

$$\hat{\mathbf{m}}^\delta dS = \det(\mathbf{F}^e)\mathbf{m}_0^\delta \cdot \mathbf{F}^{e-1} dS_0 , \tag{23}$$

where $\hat{\mathbf{m}}^\delta$ is the unit normal vector to the slip plane area element (in the current configuration), dS. Rearranging terms gives

$$\mathbf{m}_0^\delta \cdot \mathbf{F}^{e-1} = \frac{1}{\det(\mathbf{F}^e)} \frac{dS}{dS_0} \hat{\mathbf{m}}^\delta \tag{24}$$

and having expressed $\mathbf{m}^\delta$ as

$$\mathbf{m}^\delta = \mathbf{m}_0^\delta \cdot \mathbf{F}^{e-1} , \tag{25}$$

one sees that $\mathbf{m}^\delta$ is parallel to $\hat{\mathbf{m}}^\delta$. The plastic part of the velocity gradient can now be written as

$$\mathbf{L}^p = \mathbf{F}^e \cdot \mathbf{L}_i^p \cdot \mathbf{F}^{e-1} = \mathbf{F}^e \cdot \left(\sum_\delta \dot{\gamma}^\delta \mathbf{s}_0^\delta \mathbf{m}_0^\delta \right) \cdot \mathbf{F}^{e-1} = \sum_\delta \dot{\gamma}^\delta \mathbf{F}^e \cdot \mathbf{s}_0^\delta \mathbf{m}_0^\delta \cdot \mathbf{F}^{e-1} = \sum_\delta \dot{\gamma}^\delta \mathbf{s}^\delta \mathbf{m}^\delta . \tag{26}$$

It is often useful to additively decompose the velocity gradients into symmetric and antisymmetric parts as follows:

$$\mathbf{L}^e = \mathbf{D}^e + \mathbf{W}^e , \tag{27}$$

$$\mathbf{L}^p = \mathbf{D}^p + \mathbf{W}^p , \tag{28}$$

and

$$\mathbf{L}^h = \mathbf{D}^h . \tag{29}$$

The symmetric and antisymmetric parts are known as the deformation rate and spin tensors, respectively. Since the hydrogen part is purely dilatational, there is no antisymmetric part, and the velocity gradient is equal to the deformation rate tensor. For the plastic part of the deformation rate tensor, it is useful to write:

$$\mathbf{D}^p = \sum_\delta \dot{\gamma}^\delta \mathbf{P}^\delta \tag{30}$$

and

$$\mathbf{W}^p = \sum_\delta \dot{\gamma}^\delta \mathbf{Q}^\delta \tag{31}$$

where

$$\mathbf{P}^\delta = \tfrac{1}{2}(\mathbf{s}^\delta \mathbf{m}^\delta + \mathbf{m}^\delta \mathbf{s}^\delta) \tag{32}$$

and

$$\mathbf{Q}^\delta = \tfrac{1}{2}(\mathbf{s}^\delta \mathbf{m}^\delta - \mathbf{m}^\delta \mathbf{s}^\delta). \tag{33}$$

From Eqs. (19) and (21), one can show that the time rate of change of the plastic deformation gradient is given by

$$\dot{\mathbf{F}}^p = \mathbf{L}_i^p \cdot \mathbf{F}^p = \left(\sum_\delta \dot{\gamma}^\delta \mathbf{s}_0^\delta \mathbf{m}_0^\delta \right) \cdot \mathbf{F}^p . \tag{34}$$

This differential equation is integrated so that the constitutive equations may be used in the solution of the boundary value problem.

The present formulation also requires the definitions of the stress tensors to be used in the integration of the constitutive equations. In the intermediate configuration, the second Piola-Kirchhoff stress is defined as

$$\mathbf{S}^e = J\mathbf{F}^{e-1} \cdot \boldsymbol{\sigma} \cdot \mathbf{F}^{e-T} = \mathbf{F}^{e-1} \cdot \boldsymbol{\tau} \cdot \mathbf{F}^{e-T} \tag{35}$$

where $\boldsymbol{\tau} = J\boldsymbol{\sigma}$ is the Kirchhoff stress and $J = \det(\mathbf{F})$. The stress measure $\boldsymbol{\Sigma}$ is defined in the intermediate configuration as

$$\boldsymbol{\Sigma} = \mathbf{F}^{e-1} \cdot \boldsymbol{\tau} \cdot \mathbf{F}^e . \tag{36}$$

From (35), the Kirchhoff stress can be written as

$$\boldsymbol{\tau} = \mathbf{F}^e \cdot \mathbf{S}^e \cdot \mathbf{F}^{eT} \tag{37}$$

which can be substituted into (36) to give

$$\boldsymbol{\Sigma} = \mathbf{F}^{e-1} \cdot \boldsymbol{\tau} \cdot \mathbf{F}^e = \mathbf{F}^{e-1} \cdot \mathbf{F}^e \cdot \mathbf{S}^e \cdot \mathbf{F}^{eT} \cdot \mathbf{F}^e = \mathbf{S}^e \cdot \mathbf{F}^{eT} \cdot \mathbf{F}^e = \mathbf{S}^e \cdot \mathbf{C}^e \tag{38}$$

where $\mathbf{C}^e$ is the right Cauchy-Green tensor defined by $\mathbf{C}^e = \mathbf{F}^{eT} \cdot \mathbf{F}^e$.

For further understanding of the defined stress tensors, the rate of work per unit reference volume may be considered:

$$\begin{aligned} J\,\mathrm{tr}(\boldsymbol{\sigma}\cdot\mathbf{D}) &= \mathrm{tr}(\boldsymbol{\tau}\cdot\mathbf{D}) = \mathrm{tr}(\boldsymbol{\tau}\cdot\mathbf{D}^e) + \mathrm{tr}(\boldsymbol{\tau}\cdot\mathbf{D}^p) + \mathrm{tr}(\boldsymbol{\tau}\cdot\mathbf{D}^h) \\ &= \mathrm{tr}(\mathbf{F}^e\cdot\mathbf{S}^e\cdot\mathbf{F}^{eT}\cdot\mathbf{D}^e) + \mathrm{tr}(\mathbf{F}^e\cdot\mathbf{S}^e\cdot\mathbf{F}^{eT}\cdot\mathbf{D}^p) + \mathrm{tr}(\mathbf{F}^e\cdot\mathbf{S}^e\cdot\mathbf{F}^{eT}\cdot\mathbf{D}^h) \\ &= \mathrm{tr}(\mathbf{S}^e\cdot\mathbf{F}^{eT}\cdot\mathbf{D}^e\cdot\mathbf{F}^e) + \mathrm{tr}(\mathbf{S}^e\cdot\mathbf{F}^{eT}\cdot\mathbf{D}^p\cdot\mathbf{F}^e) + \mathrm{tr}(\mathbf{S}^e\cdot\mathbf{F}^{eT}\cdot\mathbf{D}^h\cdot\mathbf{F}^e). \end{aligned} \tag{39}$$

Eq. (39) can be further interpreted by considering the Green strain, given by $\mathbf{E}^e = \frac{1}{2}[\mathbf{C}^e - \mathbf{I}]$. The rate of Green strain can be written in a form that can be substituted into the first term on the right side of Eq. (39) as follows:

$$\begin{aligned} \dot{\mathbf{E}}^e &= \tfrac{d}{dt}\left[\tfrac{1}{2}(\mathbf{C}^e - \mathbf{I})\right] = \tfrac{1}{2}\dot{\mathbf{C}}^e = \tfrac{1}{2}(\dot{\mathbf{F}}^{eT}\cdot\mathbf{F}^e + \mathbf{F}^{eT}\cdot\dot{\mathbf{F}}^e) \\ &= \mathbf{F}^{eT}\cdot\tfrac{1}{2}\left[\mathbf{F}^{e-T}\dot{\mathbf{F}}^{eT} + \dot{\mathbf{F}}^e\mathbf{F}^{e-1}\right]\cdot\mathbf{F}^e = \mathbf{F}^{eT}\cdot\tfrac{1}{2}\left[\left(\dot{\mathbf{F}}^e\mathbf{F}^{e-1}\right)^T + \dot{\mathbf{F}}^e\mathbf{F}^{e-1}\right]\cdot\mathbf{F}^e \\ &= \mathbf{F}^{eT}\cdot\tfrac{1}{2}\left[\mathbf{L}^{eT} + \mathbf{L}^e\right]\cdot\mathbf{F}^e = \mathbf{F}^{eT}\cdot\mathbf{D}^e\cdot\mathbf{F}^e. \end{aligned} \tag{40}$$

The second term can be rewritten from the initial description as

$$\begin{aligned} \mathrm{tr}(\boldsymbol{\tau}\cdot\mathbf{D}^p) &= \mathrm{tr}(\boldsymbol{\tau}\cdot\mathbf{D}^p + \boldsymbol{\tau}\cdot\mathbf{W}^p) \quad \text{since} \quad \boldsymbol{\tau}\cdot\mathbf{W}^p = \mathbf{0} \quad (\boldsymbol{\tau}\ \text{symm.},\ \mathbf{W}^p\ \text{antisymm.}) \\ &= \mathrm{tr}\left[\boldsymbol{\tau}\cdot(\mathbf{D}^p + \mathbf{W}^p)\right] = \mathrm{tr}(\boldsymbol{\tau}\cdot\mathbf{L}^p) \\ &= \mathrm{tr}(\boldsymbol{\tau}\cdot\mathbf{F}^e\cdot\mathbf{L}_i^p\cdot\mathbf{F}^{e-1}) = \mathrm{tr}(\mathbf{F}^{e-1}\cdot\boldsymbol{\tau}\cdot\mathbf{F}^e\cdot\mathbf{L}_i^p) \\ &= \mathrm{tr}(\boldsymbol{\Sigma}\cdot\mathbf{L}_i^p). \end{aligned} \tag{41}$$

Letting $\dot{\mathbf{E}}^h = \mathbf{F}^{eT}\cdot\mathbf{D}^h\cdot\mathbf{F}^e$, the third term on the right hand side of Eq. (39) is written as

$$\mathrm{tr}(\mathbf{S}^e\cdot\mathbf{F}^{eT}\cdot\mathbf{D}^h\cdot\mathbf{F}^e) = \mathrm{tr}\left(\mathbf{S}^e\cdot\dot{\mathbf{E}}^h\right). \tag{42}$$

The rate of work per unit reference volume is expressed as

$$\begin{aligned} J\,\mathrm{tr}(\boldsymbol{\sigma}\cdot\mathbf{D}) &= \mathrm{tr}(\mathbf{S}^e\cdot\dot{\mathbf{E}}^e) + \mathrm{tr}(\boldsymbol{\Sigma}\cdot\mathbf{L}_i^p) + \mathrm{tr}\left(\mathbf{S}^e\cdot\dot{\mathbf{E}}^h\right) \\ &= \mathrm{tr}\left[\mathbf{S}^e\cdot(\dot{\mathbf{E}}^e + \dot{\mathbf{E}}^h)\right] + \mathrm{tr}(\boldsymbol{\Sigma}\cdot\mathbf{L}_i^p). \end{aligned} \tag{43}$$

From this expression, it is observed that $\mathbf{S}^e$ and $\boldsymbol{\Sigma}$ are respectively the elastic work rate conjugate of $\dot{\mathbf{E}}^e + \dot{\mathbf{E}}^h$ and the plastic work rate conjugate of $\mathbf{L}_i^p$.

For a hyperelastic material, the second Piola-Kirchhoff stress is derived from

$$\mathbf{S}^e = \frac{\partial\phi}{\partial\mathbf{E}^e}, \tag{44}$$

where φ is the strain energy density. Then,

$$\dot{\mathbf{S}}^e = \frac{\partial \phi}{\partial \mathbf{E}^e \partial \mathbf{E}^e} : \dot{\mathbf{E}}^e = \underset{\sim}{\mathbf{C}} : \dot{\mathbf{E}}^e \tag{45}$$

where $\underset{\sim}{\mathbf{C}}$ is the fourth-order stiffness tensor.

3.2. Hydrogen Concentration

Hydrogen atoms present in the material are assumed to reside in one of two locations: normal interstitial lattice sites (NILS) and trapping sites attributed to the plastic deformation. According to the theory of Oriani (1970), the quantities residing in each location are always in equilibrium. The following form of Oriani's equation has been adapted to account for trap sites on each slip system, δ:

$$\frac{\theta_T^\delta}{1-\theta_T^\delta} = \frac{\theta_L}{1-\theta_L} K_T, \tag{46}$$

where θ_L is the occupancy of the lattice sites, θ_T^δ is the occupancy of the trap sites on slip system δ,

$$K_T = \exp\left(\frac{W_B}{RT}\right) \tag{47}$$

denotes the equilibrium constant, W_B is the trap binding energy, $R = 8.31 \text{ J mol}^{-1} \text{ K}^{-1}$ is the gas constant, and T is the absolute temperature.

The lattice and trap hydrogen concentrations can be measured in atoms per unit volume. The lattice hydrogen concentration C_L is given by

$$C_L = \theta_L \beta N_L, \tag{48}$$

where β is the number of NILS per lattice atom and N_L denotes the number of lattice atoms per unit lattice volume. N_L is calculated from the molar volume of the lattice, V_M, through

$$N_L = N_A / V_M, \tag{49}$$

where $N_A = 6.02 \times 10^{23}$ atoms/mol is Avogadro's number.

The trapped hydrogen concentration of slip system δ, denoted by C_T^δ, is given by

$$C_T^\delta = \theta_T^\delta \alpha N_T^\delta, \tag{50}$$

where α is the number of sites per trap and N_T^δ is the trap density on slip system δ, measured in number of traps per unit volume. It is important to clarify that C_L represents hydrogen atoms residing in NILS anywhere throughout the lattice, whereas hydrogen atoms contributing to C_T^δ are trapped by dislocations that are contained in slip system δ.

To model the effects of hydrogen on the mechanical response of the single crystal, it is desirable to use a normalized form of the hydrogen concentrations. Therefore, measures of hydrogen atoms per lattice atom are introduced, first for the lattice concentration:

$$c_L = C_L / N_L, \tag{51}$$

and then for the trapped concentration on slip system δ:

$$c_T^\delta = C_T^\delta / N_L. \tag{52}$$

For the model considered in this work, the hydrogen trap sites are only associated with dislocations. Under the assumption that there exists one trap site per atomic plane threaded by a dislocation (Thomas, 1981), the trap density (in traps per unit volume) is given in terms of the dislocation density as

$$N_T^\delta = \rho^\delta / b, \tag{53}$$

where ρ^δ is the dislocation density on the δ slip plane and b is the dislocation Burgers vector. This relationship provides a crucial connection between the state of hydrogen in the material and the hardening of the crystal due to the evolving dislocation density.

At this point, it is necessary to address the treatment of the hydrogen diffusion throughout the material. In a specimen through which transient hydrogen diffusion occurs, the lattice hydrogen concentration at material points is driven by the gradient of the hydrostatic stress. In the case of a uniaxial tension test (away from the points of load application), the hydrostatic stress is uniform throughout the specimen, thus there are no hydrostatic stress peaks at which there will be significant accumulation of hydrogen. In the present work, the focus is on material systems in which the hydrogen diffusion process is very slow. For such systems, a simple calculation using a one-dimensional diffusion law can show that over the duration of a standard uniaxial tension test with a charged specimen, hydrogen could only diffuse by a negligible distance with respect to the characteristic dimensions of the specimen.

For example, to obtain insight into the distance hydrogen solute is capable of travelling during the typical uniaxial tension test duration, one-dimensional diffusion is considered in FCC nickel (which is a relatively low diffusion system in comparison to BCC iron). The one dimensional diffusion equation is given by

$$\frac{C(x,t)}{C_0} = 1 - \text{erf}\left(\frac{x}{2\sqrt{D_H t}}\right), \tag{54}$$

where $C(x,t)$ is the hydrogen concentration at position x and time t, erf is the error function, C_0 is the hydrogen concentration at a boundary that is held fixed, and $D_H = 6.6\times10^{-14}$ m^2/s is the diffusivity of hydrogen in nickel, as given by Sirois and Birnbaum (1992). In the experiment done by Yagodzinskyy et al. (2009) with pure nickel, the duration of the test was about 13 minutes, and the specimen dimensions were $0.3\times5\times8$ mm. Based on the duration of the test, it can be shown that the concentration is less than half a percent of C_0 at a distance of 29 microns, which is far smaller than the minimum dimension of a typical specimen. A comparison can be made to research performed by Somerday et al. (2009) on austenitic stainless steels in which the total hydrogen concentration in hydrogen-charged specimens was found to be relatively unchanged as hydrogen only diffused over extremely short distances during the test. However, it should be noted that while the bulk hydrogen diffusion is very slow, the interchange of hydrogen between NILS and trap sites can be significant due to the intense plastic straining and associated trap (dislocation) generation.

From the physically-based assumption that the total hydrogen concentration is constant at each material point in the specimen throughout the duration of the uniaxial tension test, the following relation should be satisfied:

$$C_L + \sum_{\delta} C_T^{\delta} = C_0, \tag{55}$$

where C_0 is the total hydrogen concentration before the application of any load (stress-free lattice). This equation can also be expressed in terms of the normalized concentrations simply by dividing all terms by N_L.

Since the total hydrogen concentration at a material point is constant, Eq. (14) reduces as

$$\mathbf{F}^h = \left(1 + \frac{(c - c_0)\lambda}{3}\right)\mathbf{I} = \left(1 + \frac{(0)\lambda}{3}\right)\mathbf{I} = \mathbf{I} \tag{56}$$

i.e. the hydrogen part of the deformation gradient becomes the identity tensor. Since the time rate of change of the identity tensor is zero, the hydrogen part of the velocity gradient will vanish, as will the hydrogen part of the deformation rate tensor.

3.3. Model of the Hydrogen Effect on the Plastic Flow

As previously mentioned, plastic deformation will occur on a given slip system when the yield criterion is met on that system; this criterion can be evaluated using a generalization of Schmid's law (Hill, 1966). For a slip system to be potentially active, the following criterion must be satisfied:

$$\tau^\delta - \tau_{cr}^\delta = 0 \tag{57}$$

where τ^δ and τ_{cr}^δ are the resolved shear stress and critical resolved shear stress, respectively, on slip system δ. The resolved shear stress is defined in terms of the Kirchhoff stress, $\boldsymbol{\tau} = J\boldsymbol{\sigma}$, as

$$\tau^\delta = \mathbf{m}^\delta \cdot \boldsymbol{\tau} \cdot \mathbf{s}^\delta . \tag{58}$$

Eq. (36) can be substituted into Eq. (58) to obtain

$$\tau^\delta = \mathbf{m}^\delta \cdot \mathbf{F}^e \cdot \boldsymbol{\Sigma} \cdot \mathbf{F}^{e-1} \cdot \mathbf{s}^\delta , \tag{59}$$

and applying Eqs. (22) and (25) yields

$$\tau^\delta = \mathbf{m}_0^\delta \cdot \boldsymbol{\Sigma} \cdot \mathbf{s}_0^\delta . \tag{60}$$

Eq. (57) can now be expressed as

$$\mathbf{m}_0^\delta \cdot \boldsymbol{\Sigma} \cdot \mathbf{s}_0^\delta - \tau_{cr}^\delta = 0 . \tag{61}$$

A description of the evolution equations for the critical resolved shear stress has been given in Subsection 2.1. For the present model, an equation that is capable of capturing the observed hydrogen effects on single crystals is desired. The classical relations given in Eqs. (2) and (4) can be combined to give the following evolution equation based on the bulk dislocation density:

$$\dot{\tau}_{cr} = \left(H - R\tau_{cr}\right)\dot{\gamma} , \tag{62}$$

where $H = \alpha' \mu b c_1 / 2$ and $R = c_2 / 2$ represent the hardening and recovery parameters, respectively. Based on experimental observations, dislocation recovery becomes a significant factor in stage III, but it does not contribute dramatically in stages I and II. In the present model, a greater emphasis is placed on capturing the behaviors of the first two stages. In the generalization of Eq. (62) to the case of multislip, the absence of significant recovery in the early stages is considered and the model takes the following form:

$$\dot{\tau}_{cr}^{\delta} = \left[H^{\delta} - R^{\delta} \left(\tau_{cr}^{\delta} - \tau_0 \right) \right] \dot{\gamma}^{\delta} \tag{63}$$

where H^{δ} and R^{δ} are hardening and recovery parameters, respectively, on slip system δ. It is expected that these parameters will be dependent on the hydrogen effect on dislocations outlined in Subsection 2.2. Note that the recovery parameter, R^{δ}, is the coefficient to the amount by which the critical resolved shear stress on a given slip plane exceeds the initial critical resolved shear stress, τ_0, and thus the recovery term has no initial effect at the onset of plastic deformation.

Since the early hardening behavior is divided into two distinct regions (stage I and stage II), it is reasonable to consider incorporating a piecewise function into the evolution equation. Stage I is characterized by small hardening or no hardening and stage II is characterized by near-linear hardening. Typically, the hardening in stage II is one order of magnitude larger than the hardening in stage I (Kocks and Mecking, 2003); this escalation of the hardening can be captured by a piecewise function provided that the transition between the two stages is correctly identified. In fact, this point can easily be recognized by the activation of additional slip systems (beyond the primary slip system).

Inspired by the work of Bassani and Wu (1991), a model is proposed that will account for the sharp increase in hardening as well as the varying strengths of slip system interactions. A piecewise function may be appended onto Eq. (63) to capture this sharp increase in hardening:

$$\dot{\tau}_{cr}^{\delta} = \left[H^{\delta} \begin{Bmatrix} 1 & \text{for } n = 1 \\ 1 + F_{II} \sum\limits_{\substack{\beta \\ \beta \neq \delta}} f_{\delta\beta} & \text{for } n > 1 \end{Bmatrix} - R^{\delta} \left(\tau_{cr}^{\delta} - \tau_0 \right) \right] \dot{\gamma}^{\delta} \tag{64}$$

where n is the number of active slip systems, F_{II} is a parameter between 0 and 1, $[f_{\delta\beta}]$ is the interaction matrix found in Eq. (10), and the summation is carried out over all active slip systems β such that $\beta \neq \delta$. The piecewise function is applied only to the hardening parameter as there is no evidence that the dislocation-dislocation interactions represented by the interaction matrix apply to recovery. When $F_{II} = 1$, the appended piecewise function is in agreement with the large strain asymptote of the function, G, given in Eq. (10). When $F_{II} = 0$, Eq. (64) reduces to the form of Eq. (63).

In choosing functions to model the parameters involved with the hardening equation, it is necessary to recall the significant effects that hydrogen has been shown to have on single crystal specimens. In particular, the following characteristics should be within the scope of the parameters (as functions of the hydrogen concentration) in order to capture the correct constitutive response when hydrogen is present:

1. The duration of stage I is extended by the presence of hydrogen compared to the hydrogen-free material.
2. The initial yield stress of the specimen increases up to about 20%.

Though these points are not inclusive of all the effects that hydrogen has on single crystal specimens, these characteristics represent a minimal basis that a sufficient model should be able to capture. The choices of the functions for the parameters involved in the hardening model are based on satisfying these requirements without choosing an overly complex way of including the effect of hydrogen.

For the purpose of this study, these functions have been chosen to demonstrate the appropriate effect of hydrogen on the deformation; further adjustments and modifications are easily applied as experimental evidence presents itself to justify such changes. First, the hardening parameter can be expressed as a function of the hydrogen concentration through

$$H^{\delta} = H^{\delta}(c_T^{\delta}) = H_0\left(1 + H_C c_T^{\delta}\right) \tag{65}$$

where H_0 is the hydrogen-free hardening parameter, H_C is a dimensionless parameter that governs the magnitude of the hydrogen effect on hardening, and c_T^{δ} is the concentration of hydrogen atoms per lattice atom trapped at dislocations on slip system

δ. In the hardening parameter, as with the other parameters, it is assumed that only the trapped hydrogen affects the dislocation response. Similarly to the hardening parameter, the recovery parameter can be defined as a function of the hydrogen concentration through

$$R^{\delta} = R^{\delta}(c_T^{\delta}) = R_0\left(1 + R_C c_T^{\delta}\right) \tag{66}$$

where R_0 is the hydrogen-free recovery parameter and R_C is a dimensionless parameter that governs the effects of hydrogen on recovery.

Finally, it is important to recall the effect of hydrogen on the initial yield stress in uniaxial tension. The initial critical resolved shear stress can be expressed as a function of the trapped hydrogen concentration through

$$\left(\tau_{cr}^{\delta}\right)_{initial} = \tau_0\left(1 + T_C c_T^{\delta}\right) \tag{67}$$

where τ_0 is the hydrogen-free critical resolved shear stress and T_C is the dimensionless parameter that governs the effects of hydrogen on the initial yielding. Based on the experimental observations, the initial critical resolved shear stress should be an increasing function of c_T^{δ}; therefore, T_C takes values that are greater than zero.

4. Simulation and Model Validation

The present work specifically focuses on the simulation of FCC single crystals. In FCC single crystals, the crystallographic structure is defined by 12 independent slip systems (24 when positive and negative directions are counted separately). These slip systems are given in Table 1, along with the indices by which they are referenced. Under the assumption that there is no Bauschinger effect, the values for τ_{cr}^{α} are the same for both positive and negative directions on a given slip system. The values for c_T^{α} are also assumed to be independent of the sign of the direction on a given slip system. For most of the simulations in this work, the material properties for nickel single crystals are used; these are given in Table 2. Simulations are also conducted to compare the present model to that of Bassani and Wu (1991), for which case material properties for copper single crystals are used; these properties are given in Table 3.

Simulations are performed using a user subroutine in Abaqus/Standard defining the material behavior (known as a UMAT). The mesh consists of a single 8-node linear brick element (C3D8 as denoted in Abaqus). The code for the subroutine is based on the crystal plasticity framework outlined in Section 3. The tangent modulus, which is used by Abaqus in satisfying equilibrium, is derived in Appendix C. The boundary conditions for the mesh and the applied loading are shown in Fig. 2. Due to the anisotropic behavior of single crystals, it is necessary to apply a load-controlled boundary conditions rather than a displacement-controlled boundary conditions. In fact, the use of displacement-controlled boundary conditions would result in excessive constraints of the deformation and artificial effects on the stress-strain curve. This problem is also evident in experimental testing of single crystals; most types of displacement-controlled testing apparatus apply an axial displacement while constraining transverse displacements. Research done by Lassilla and coworkers (Florando et al., 2007; Lassila et al., 2007) on single crystal specimens have addressed this issue through the design of a "6 degrees of freedom" apparatus that does not restrict the transverse displacements or rotations at the surfaces of load application. Though these tests are performed in compression rather than tension, the issue of crystal anisotropy that it addresses is identical in nature and should

be addressed in any axial tension test of single crystals to avoid erroneous and misleading results.

Numerous simulations are conducted using the outlined constitutive model. The slip system (or systems) that are initially activated can be determined from the orientation of the tensile axis using a stereographic projection for an FCC metal crystal. The stereographic projection from Kelly and Groves (1970) is use to verify the slip systems that are initially activated for various tensile axis orientations. For a qualitative comparison with the results of Yagodzinskyy et al. (2009) on single crystal nickel specimens, the tensile axis is chosen to be aligned with the $[\bar{1}67]$-direction. The stereographic projection mentioned above is used to predict that the $(111)[\bar{1}01]$ slip system is the primary slip system that is initially activated for the given tensile axis orientation. This slip system is found to be the primary slip system in the numerical simulation as well.

Parametric studies are performed by varying the parameters that dictate the hardening behavior of the crystal specimen, including H_0, H_C, R_0, R_C, and T_C. The calibration made using the experimental results serves as a starting point from which the above parameters can be varied. From these variations, a better understanding of how hydrogen affects the macroscopic simple uniaxial tension response can be obtained.

5. Results for Uniaxial Tension of a Single Crystal

5.1. Numerical Verification

To verify the accuracy of the numerical methods used to implement the constitutive model proposed in this work, uniaxial tension simulations are conducted on single crystals in which only one slip system is allowed to become active. Since only one slip system is active, the superscript Greek character is dropped in this subsection. For this special case, an analytical solution to the differential equation governing the evolution of the critical resolved shear stress can be obtained, and this can be compared to the numerical results. The exact analytical solution is given in Appendix D. Analytical and numerical shear stress-shear strain curves for the active slip system are shown in Fig. 3 for the test case with $\tau_0 = 20$ MPa, $H_0 = 125$ MPa, and $R_0 = 4$. Agreement between the analytical and numerical solutions is shown up to a shear strain of 0.1. Although only one slip system is active, the solution represents a general result for any active slip system, regardless of tensile axis orientation, for the case of single slip in the absence of hydrogen.

The validity of the yield condition is checked by calculating the critical applied stress based on the critical resolved shear stress at which the onset of plastic deformation occurs. The calculated value of the applied stress is then compared with the value found numerically using the model. This can be checked for any model in which a single slip system is initially active. For the purposes of validation, a model with only one slip system (rather than the 12 found in FCC crystals) is used so that the slip system orientation relative to the tensile axis is more clearly measured. Several tests are done with varying slip system orientation, θ. The definition of θ as well as the definition of the axes is found in Fig. 2. The resolved shear stress, τ, on the active slip system is calculated using the stress transformation equation for shear stress:

$$\tau = -\frac{(\sigma_{22} - \sigma_{33})}{2}\sin 2\theta + \tau_{23}\cos 2\theta . \tag{68}$$

Based on the defined orientation, σ_{22} and τ_{23} vanish in the reference configuration for the simple uniaxial tension test. The applied stress, σ_{33}, at which the resolved shear

stress equals the critical resolved shear stress, τ_{cr}, is then determined from (68) as follows:

$$\tau_{cr} = -\frac{(0-\sigma_{33})}{2}\sin 2\theta + (0)\cos 2\theta = \frac{\sigma_{33}}{2}\sin 2\theta \Rightarrow \sigma_{33} = \frac{2\tau_{cr}}{\sin 2\theta}. \qquad (69)$$

Table 4 shows a comparison of the analytical and numerical results for the initial yielding, and good agreement is found between the two.

5.2. Comparison to Bassani and Wu Hardening Model

As described in Subsection 2.2, the Bassani and Wu (BW) hardening model was shown to capture the behavior of single crystals in uniaxial tension (Bassani and Wu, 1991). Since the present model is aiming to capture stage I and the onset of stage II, certain qualitative comparisons can be made between these two models. In particular, the tensile axis orientations $[321]$ and $[632]$ are of interest since these orientations allow for a significant easy glide region. For the sake of agreement with the BW model, the values for the elastic properties as well as the initial critical resolved shear stress, τ_0, for copper single crystals are used (see Table 3).

The plots of the critical resolved shear stress versus shear strain for these two tensile axis orientations are shown in Figs. 4 and 5. The values for the critical resolved shear stress and shear strain correspond to the slip system #23 (see indexing in Table 1) since this is the slip system that is initially activated in easy glide for both orientations. Other slip systems become active during stage II, but since the goal of the model is to capture stage I and the onset of stage I, the nature of the curves corresponding to these secondary slip systems is of less concern. For the present model, the parameter H_0, which is in general fixed for a given material, is set to 37.5 MPa to best match the general character of the BW model, and the stage II parameter F_{II} is set to 1.0.

It should be noted that based on the hardening equation used for primary slip in the BW model, there is a short period of high initial hardening. This highly nonlinear behavior is not immediately captured by the present model; however, by beginning with an initially elevated critical resolved shear stress, good agreement is still found between the BW model and the present model. For the $[321]$ orientation in Fig. 4, the initial

critical resolved shear stress is increased by 30%, and for the $[632]$ orientation in Fig. 5, it is increased by 40%.

5.3. Model Calibration: The Hydrogen Effect on Nickel Single Crystals

In order to calibrate the present model, it is desirable to use experimental data from single crystal specimens in uniaxial tension in which the necessary parameters are readily available. The stress-strain curves produced by Yagodzinskyy et al. (2009) for single crystal nickel specimens provide a useful point for calibration. This particular calibration is used for reasonable qualitative results for straining of hydrogen charged specimens, though the accuracy of the quantitative data cannot be assured. As such, much care has been taken that the capabilities of the model described here be related to physical mechanisms at the root of the hydrogen-dislocation interactions. The experimental results are useful in obtaining a beginning set of parameters that can be varied to further explore the sensitivities of the model.

The following characteristics are identified from the experimental results of Yagodszinskyy et al. as important considerations for the calibration:

1. The yield stress in uniaxial tension of the hydrogen-free single crystal specimen is approximately 40 MPa; the yield stress for the hydrogen-charged single crystal is about 20% higher than the hydrogen-free single crystal.
2. The onset of stage II in the hydrogen-charged specimen is found to occur at up to 100% greater axial strain than in the hydrogen-free specimen.

The parameter values that are found to adequately meet the above conditions are given in Table 5, along with the hydrogen concentrations and other pertinent parameters used for the calibration. Of particular note is the initial (hydrogen-free) critical resolved shear stress, $\tau_0 = 18.3$ MPa , which is chosen such that the macroscopic yield stress in uniaxial tension for the present model matches that of the BW model. From the critical resolved shear stress, an approximate calculation of the dislocation density can be made from Eq. (2), yielding $\rho = 8.11\times10^{12}$ dislocations per square meter. Then, the initial total number of traps per unit volume is found using Eq. (53) (and taking into account all 12 slip systems for the FCC crystal) to be $\left(N_T\right)_{initial} = 3.255\times10^{20}$ traps/m^3 . The recovery

parameters R_0 and R_C are chosen to be zero since the recovery terms have a small effect on stage I and stage II. Finally, since the lattice hydrogen concentration is not given for the tests conducted by Yagodzinskyy et al., a value of $c_L = 0.015$ hydrogen atoms per lattice atom, which is typical of hydrogen-charging in stainless steels, is used (Somerday et al., 2009).

Axial stress-strain curves are given in Fig. 6 for the calibrated model and the experiment. The stage II parameter, F_{II}, is set to 0.5 to better match the experimental data. The plot of the critical resolved shear stress versus shear strain on the slip system that becomes active in stage I is given in Fig. 7. The critical resolved shear stress and shear strain are given for the $(111)[\bar{1}01]$ system, the system that is initially active as described above. In stage II, the $(1\bar{1}\bar{1})[\bar{1}0\bar{1}]$ and $(111)[\bar{1}10]$ system are also activated. For the hydrogen-charged single crystal simulation, the trapped hydrogen atoms per lattice atom, c_T, on these slip systems is shown in Fig. 8 as a function of the axial strain. The initial value of c_T on each slip system is calculated using the hydrogen equations in Subsection 3.2 and the parameters in Table 5; for the present model, the initial value of c_T on each system is approximately 0.2×10^{-6} hydrogen atoms per lattice atom.

5.4. Parametric Studies for the Hydrogen Effect on Nickel Single Crystals

Studies are done on the variation of the stress-strain behavior of nickel single crystals oriented to exhibit stage I for various values of H_C, R_C, and T_C. The range through which these parameters are varied is chosen to include values that would correspond to an extreme effect due to hydrogen as well as values corresponding to no hydrogen effect. For consistency, the tensile axis orientation is set to the $[\bar{1}67]$-direction to match the calibration described in the preceding subsection. The slip systems active in stage I and stage II are therefore identical to the previous case. The stage II parameter, F_{II}, is set to 1.0 throughout these simulations to reflect the significant increase in hardening in stage II.

The stress-strain curves for varying magnitudes of the hardening parameter, H_0, are shown in Fig. 9. The onset of stage II occurs at nearly the same applied stress for

each different value of the hardening parameter, but as the magnitude of the hardening parameter increases, the axial strain at which the onset of stage II occurs decreases. The duration of stage I hardening is clearly dependent on the choice of this hardening parameter, and as the stage I hardening decreases to the minimal values observed in the experiment (see Fig. 6), the duration of stage I is found to increase dramatically.

Figs. 10 and 11 show the effect of the variation in the coefficient of the hydrogen effect on hardening, H_C. The range of values for which simulations are carried out include both positive and negative values, which would correspond to an increase and decrease in hardening, respectively, due to the presence of hydrogen. The curve for $H_C = 0$ corresponds to the hydrogen-free case. Fig. 11 shows a magnified view of the transition from stage I to stage II, as this transition is very important in predicting the hydrogen effect on the deformation.

To investigate the effect of the recovery term on the stress-strain behavior, the variation of the recovery parameter, R_0, is first considered. Fig. 12 shows the stress-strain curves for varying values of R_0 in the absence of hydrogen. The recovery parameter is varied from no recovery ($R_0 = 0$) to significant recovery ($R_0 = 8$). It is observed that an increase in the recovery parameter will prolong stage I, similarly to the effect seen when decreasing the hardening parameter. Fig. 13 shows the stress strain curves for variation of R_0 for the hydrogen-charged specimen using the same range of values for R_0 as the hydrogen-free case.

Having introduced a nonzero recovery parameter, the effect of hydrogen on recovery through the coefficient R_C is now considered. The stress-strain curves for a range of values of R_C are shown in Fig. 14. This range encompasses both positive and negative values for the recovery, particularly due to the absence of a thorough physical understanding of the type of effect that hydrogen has on the recovery. Since a nonzero recovery parameter is required to observe the effect of varying R_C, $R_0 = 4$ is used for these stress-strain curves.

Stress-strain curves corresponding to the variation of the coefficient of the hydrogen effect on the initial critical resolved shear stress, T_C, are given in Fig. 15.

Based on experimental observations of single crystal nickel specimens, the coefficient is always taken to be positive. It is varied from no effect of hydrogen on the initial critical resolved shear stress ($T_C = 0$) to a severe effect ($T_C = 3\times10^6$) (high initial hardening is based on a concentration of trapped hydrogen atoms per lattice atom of about 0.2×10^{-6}). An increase in macroscopic yield stress of nearly 50% is observed for the choice of $T_C = 3\times10^6$. The presence of hydrogen increases the initial critical resolved shear stress on all slip systems uniformly, so an increased T_C causes the onset of stage I as well as the onset of stage II to occur at a higher applied stress, σ_{33}. The onset of stage II also occurs at a larger value of axial strain, which is equivalent to observing a prolonged stage I; for the case of $T_C = 3\times10^6$, the duration of stage I increases by around 75% compared to the case of $T_C = 0$.

6. Discussion

Based on the parametric studies described in Subsection 5.4, the results for hydrogen-free and hydrogen-charged specimens can be interpreted. For both cases, the duration of each stage of hardening as well as the rate of hardening seem to be intimately related to the varied parameters H_0, H_C, R_0, R_C, and T_C. From the comparisons made in Fig. 6 between model predictions and experimental data, it seems that decreasing the hardening parameter, H_0, will lead to closer agreement with the minimal hardening seen in the experimental results. However, decreasing the hardening parameter is found to cause the onset of stage II to occur at larger strains than in the experiment, as can be seen in Fig. 9. As a result, the hardening parameter has been chosen such that the strain at which the onset of stage II occurs in the model matches the experiment at the loss of exactly matching the rate of hardening seen in stage I.

The recovery parameter, R_0, is seen to have a noticeable effect on stage I in Figs. 12 and 13, though significant effects of recovery are not observed in stage I in experimental studies. The effect of recovery is not as apparent in stage II due to the sharp increase in the hardening parameter. This result seems to agree with the observed recovery, or lack thereof, in experimental studies. Based on the above observations, it seems reasonable to suggest that the recovery parameter may be removed from Eq. (64) for stage I. This could be carried out similarly to the application of the piecewise function applied to the hardening terms to simulate increased hardening in stage II. Such a modification would allow the recovery term to remain in stage II, though the effect would be small, while also allowing for stage III recovery to be readily accounted for upon further revision of the model.

Details of the effect of hydrogen on the characteristics of the stress-strain curve are also to be considered. It can be seen that a reduction in hardening in stage I due to hydrogen is able to account for the delayed onset of stage II. Though the increased duration of stage I is largely controlled by varying of the coefficient for the hydrogen effect on hardening, H_C, it is also observed that modification of the parameters

controlling the hydrogen effect on the initial critical resolved shear stress and dislocation recovery have a noticeable effect on when the onset of stage II occurs.

The decrease in H_C can be associated with the increased dislocation velocity due to the presence of hydrogen. The elevation of the initial macroscopic yield stress in uniaxial tension through the increase in the initial critical resolved shear stress attributed to hydrogen has been be related to the locking of Frank-Read and other dislocation sources. As for the recovery parameters, present experimental data does not give a complete understanding of the effect that hydrogen has on recovery. However, it is to be noted that the results by Ferreira et al. (1998) and Robertson (2001) suggest that the recovery is inhibited by the presence of hydrogen. Since the recovery becomes a more significant factor in stage III, it would be useful to obtain experimental data with single crystal uniaxial tension on hydrogen-free and hydrogen charged specimens exhibiting clear stage III hardening. Since most of the hydrogen effects for polycrystalline systems are observed upon yielding, it seems that our present model provides a sufficient framework to understand the hydrogen effect on the mechanical response.

7. Summary and Future Work

The model that has been presented in this work represents the beginning of a potentially extensive implementation of the knowledge of the hydrogen-dislocation interactions within a crystal plasticity framework. The inclusion of the hydrogen-dependence within the hardening and flow stress equations yields a crystal plasticity constitutive model that can be instrumental in developing finite element procedures that can handle more complicated problem definitions and geometries that involve hydrogen and its effect on the deformation of FCC metals and alloys. The parametric studies conducted present a range of capabilities in simulating various effects that hydrogen has been shown to have on single crystal specimens as well as more general bulk material response.

Based on the formulation of the problem and the structure of the user material subroutine, the present constitutive model used can be modified as developments occur. The treatment of the dislocation density should be considered in any future changes. In particular, since hydrogen has been observed to increase dislocation velocity (Robertson, 2001), it is desirable to construct a model that will take this effect into account directly. Kubin et al. (2008) present a possible link through which these modifications may be applied.

One of the most difficult challenges pertaining to the single crystal uniaxial tension problem is applying the deformation in such a way that the near zero hardening stage I seen in the experimental results can be captured by the model. As discussed in Section 4, a displacement-controlled deformation can over-constrain axial degrees-of-freedom, preventing a state of uniaxial tension in the specimen; to preserve a state of uniaxial tension, a load-controlled deformation must be applied. The load-controlled deformation, however, is restricted in the sense that the hardening needs to be finite and positive, which excludes the possibility of having a zero (or near zero) slope region in the stress-strain curve. Solutions to this problem may require implementing a displacement-controlled deformation in a way that is somehow less restrictive on the degrees of freedom of the specimen. Such a simulation may be carried out through modeling the "6 degrees of freedom" apparatus mentioned previously (Lassila et al., 2007). Another

viable option is to modify the numerical methods so that a stable solution can be found as the hardening essentially approaches zero.

The formulation of the single crystal constitutive model provides a critical component for the ongoing investigation of the hydrogen-dislocation interactions in polycrystalline metals as well as more complex boundary value problems for single crystals. This model allows for consideration of the unique anisotropic behavior of single crystals as they are subject to hydrogen. Though this model has been constructed for a single crystal, a polycrystalline model that incorporates the present constitutive model for individual crystals may provide new avenue for understanding the effect of hydrogen in a more general class of materials. The use of the single crystal model in different boundary value problems, such as the crack-tip problem, can provide insight into the effect of crystal mechanisms on macroscopically observed behaviors.

This thesis presents a versatile approach to the constitutive response of single crystals and how this response is affected by the presence of hydrogen. The constitutive model has demonstrated the ability to adequately describe and capture the experimentally-observed hydrogen effects on single crystals. In particular,

- The increase of the yield stress in uniaxial tension as affect by hydrogen.
- The delay of the onset of stage II hardening, i.e. the increase of the duration of stage I.
- The hydrogen effects on hardening and recovery.

The treatment of the constitutive model in the context of the hydrogen-dislocation interactions provides a physical basis for the parameters that have been employed in the model. These parameters have been designed based on the effect of hydrogen on the hardening, recovery, and yield strength, and continued research on hydrogen-charged single crystals will provide useful data for discerning the magnitudes of these parameters. The detailed investigation of the sensitivity of the model to the variation of these parameters provides a foundation for expanding the predictive capabilities of the model in future works.

8. References

Abraham, D.P. and C.J. Altstetter, 1995. "The effect of hydrogen on the yield and flow stress of an austenitic stainless steel." *Metallurgical and Materials Transactions A*. 26, pp. 2849-2858.

Aravas, N., 1991. "On the geometry of slip and spin in finite plastic deformation." *International Journal of Plasticity*. 7, pp. 141-160.

Aravas, N., 1994. "Finite-strain anisotropic plasticity and the plastic spin." *Modelling and Simulation in Materials Science and Engineering*. 2, pp. 483-504.

Bassani, J.L and T. Wu, 1991. "Latent hardening in single crystals II. Analytical characterization and predictions." *Proceedings of the Royal Society of London A*. 434, pp. 1-19.

Beachem, C.D., 1972. "A new model for hydrogen-assisted cracking (hydrogen 'embritttlement')." *Metallurgical and Materials Transactions B*. 3, pp. 437-451.

Birnbaum, H.K. and P. Sofronis., 1994. "Hydrogen-enhanced localized plasticity—a mechanism for hydrogen-related fracture." *Materials Science & Engineering A*. 176, pp. 191-202.

Birnbaum, H.K., I.M. Robertson, P. Sofronis, and D. Teter, 1997. "Mechanisms of hydrogen related fracture—A review," in: Magnin, T. (ed.), *Corrosion Deformation Interaction CDI'96, Second International Conference*. The Institute of Materials, Great Britain, pp. 172-195.

Delafosse, D., X. Feaugas, I. Aubert, N. Saintier, and J.M. Olive, 2009. "Hydrogen Effects on the Plasticity of FCC Nickel and Austenitic Alloys." *Proceedings of the 2008 International Hydrogen Conference*. B. Somerday, P. Sofronis, and R. Jones, eds., pp. 78-87.

Devincre, B., T. Hoc, and L. Kubin, 2008. "Dislocation Mean Free Paths and Strain Hardening of Crystals." *Science*. 320, pp. 1745-1748.

Estrin, Y. and H. Mecking, 1984. "A unified phenomenological description of work hardening and creep based on one-parameter models." *Acta Metallurgica*. 32, pp. 57-70.

Ferreira, P.J., I.M. Robertson, and H.K. Birnbaum, 1999. "Hydrogen effects on the character of dislocations in high-purity aluminum." *Acta Materialia*. 47, pp. 2991-2998.

Florando, J.N., M.M. LeBlanc, and D.H. Lassila, 2007. “Multiple slip in copper single crystals deformed in compression under uniaxial stress.” *Scripta Materialia*. 57, pp. 537-540.

Hill, R., 1966. “Generalized constitutive relations for incremental deformation of metal crystals by multislip.” *Journal of the Mechanics and Physics of Solids*. 14, pp. 95-102.

Hirth, J.P., 1980. “Effects of hydrogen on the properties of iron and steel.” *Metallurgical and Materials Transactions A*. 11, pp. 861-890.

Kelly, A. and G.W. Groves, 1970. *Crystallography and Crystal Defects*. Addison-Wesley Publishing Company. Reading, Massachusetts.

Kimura, A. and H.K. Birnbaum, 1987. “Plastic softening by hydrogen plasma charging in pure iron.” *Scripta Metallurgica*. 21, pp. 53-57.

Kocks, U.F. and H. Mecking, 2003. “Physics and phenomenology of strain hardening: the FCC case.” *Progress in Materials Science*. 48, pp. 171-273.

Kubin, L., B. Devincre, and T. Hoc, 2008. “Modeling dislocation storage rates and mean free paths in face-centered cubic crystals.” *Acta Materialia*. 56, pp. 6040-6049.

Lassila, D.H., M.M. LeBlanc, and J.N. Florando, 2007. “Zinc-Single Crystal Deformation Experiments Using a ‘6 Degrees of Freedom’ Apparatus.” *Metallurgical and Materials Transactions A*. 38, pp. 2024-2032.

Lee, E.H., 1969. “Elastic-plastic deformation at finite strains.” *Journal of Applied Mechanics*. 36, pp. 1-6.

Matsui, H., H. Kimura, and S. Moriya, 1979a. “The effect of hydrogen on the mechanical properties of high purity iron I. Softening and hardening of high purity iron by hydrogen charging during tensile deformation.” *Materials Science and Engineering*. 40, pp. 207-216.

Matsui, H., H. Kimura, and A. Kimura, 1979b. “The effect of hydrogen on the mechanical properties of high purity iron III. The dependence of softening in specimen size and charging current density.” *Materials Science and Engineering*. 40, pp. 227-234.

Moriya, S., H. Matsui, and H. Kimura, 1979. “The effect of hydrogen on the mechanical properties of high purity iron II. Effect of quenched-in hydrogen below room temperature.” *Materials Science and Engineering*. 40, pp. 217-225.

Peisl, H., 1978. “Lattice strains due to hydrogen in metals.” *Hydrogen in Metals I, Topics in Applied Physics*. 28, pp. 53-74.

Robertson, I.M. and H.K. Birnbaum, 1986. "An HVEM study of hydrogen effects on the deformation and fracture of nickel." *Acta Metallurgica*. 34, pp. 353-366.

Robertson, I.M., 2001. "The effect of hydrogen on dislocation dynamics." *Engineering Fracture Mechanics*. 68, pp. 671-692.

Sirois, E. and H.K. Birnbaum, 1992. "Effects of hydrogen and carbon on thermally activated deformation in nickel." *Acta Metallurgica et Materialia*. 40, pp. 1377-1385.

Sofronis, P. and H.K. Birnbaum, 1995. "Mechanics of the hydrogen-dislocation-impurity interactions—I. Increasing shear modulus." *Journal of the Mechanics and Physics of Solids*. 43, pp. 49-90.

Somerday, B.P., M. Dadfarnia, D.K. Balch, K.A. Nibur, C.H. Cadden, and P. Sofronis, 2009. "Hydrogen-Assisted Crack Propagation in Austenitic Stainless Steel Fusion Welds." *Metallurgical and Materials Transactions A*. 40, pp. 2350-2362.

Tabourot, L., M. Fivel, and E. Rauch, 1997. "Generalized constitutive laws for f.c.c. single crystals." *Materials Science and Engineering A*. 234-236, pp. 639-642.

Taylor, G.I., 1934. "The Mechanism of Plastic Deformation of Crystals. Part I. Theoretical." *Proceedings of the Royal Society A*. 145, pp. 362-387.

Thomas, G.J., 1981. "Hydrogen trapping in FCC metals." *Hydrogen Effects in Metals*. I.M. Bernstein and A.W. Thompson, eds. pp. 77-84.

Ulmer, D.G. and C.J. Altstetter, 1991. "Hydrogen-induced strain localization and failure of austenitic stainless steels at high hydrogen concentrations." *Acta Metallurgica et Materialia*. 39, pp. 1237-1248.

Yagodzinskyy, Y., O. Tarasenko, and H. Hänninen, 2003. "Effect of hydrogen on plastic deformation of stable 18Cr-16Ni-10Mn austenitic stainless steel single crystals." *Hydrogen Effects on Material Behavior and Corrosion Deformation Interactions*. N.R. Moody, A.W. Thompson, R.E. Ricker, G.W. Was, and R.H. Jones, eds. pp. 201-210.

Yagodzinskyy, Y., T. Saukkonen, H. Hänninen, F. Tuomisto, S. Barannikova, and L. Zuev., 2009. "Effect of Hydrogen on Plastic Strain Localization in Single Crystals of Nickel and Austenitic Stainless Steel." *Proceedings of the 2008 International Hydrogen Conference*. B. Somerday, P. Sofronis, and R. Jones, eds., pp. 97-104.

9. Tables

Table 1. Slip systems for FCC model (including positive and negative directions) with indices as referenced in the Abaqus UMAT.

Index	Slip normal	Slip direction	Index	Slip normal	Slip direction
1		$[01\bar{1}]$	13		$[0\bar{1}1]$
2	(111)	$[\bar{1}01]$	14	(111)	$[10\bar{1}]$
3		$[1\bar{1}0]$	15		$[\bar{1}10]$
4		$[0\bar{1}1]$	16		$[01\bar{1}]$
5	$(1\bar{1}\bar{1})$	$[\bar{1}0\bar{1}]$	17	$(1\bar{1}\bar{1})$	$[101]$
6		$[110]$	18		$[\bar{1}\bar{1}0]$
7		$[011]$	19		$[0\bar{1}\bar{1}]$
8	$(\bar{1}1\bar{1})$	$[10\bar{1}]$	20	$(\bar{1}1\bar{1})$	$[\bar{1}01]$
9		$[\bar{1}\bar{1}0]$	21		$[110]$
10		$[0\bar{1}\bar{1}]$	22		$[011]$
11	$(\bar{1}\bar{1}1)$	$[101]$	23	$(\bar{1}\bar{1}1)$	$[\bar{1}0\bar{1}]$
12		$[\bar{1}10]$	24		$[1\bar{1}0]$

Table 2. Material properties for single crystal nickel.

Parameter	Value	Definition	Source
		Hydrogen Diffusion	
W_B	9.56 kJ/mol	trap binding energy	Thomas, 1981
R	8.31 J/mol K	gas constant	
T	300 K	absolute temperature	
$K_T = \exp\left(\frac{W_B}{RT}\right)$	46.28	equilibrium constant	(calculated from above parameters)
α	1.0	number of sites per trap	Sofronis et al., 2001
β	1.0	number of interstitial lattice sites per lattice atom	Sofronis et al., 2001
V_M	6.59×10^{-6} m^3 / mol	molar volume of nickel	
N_L	9.14×10^{28} atoms/m^3	number of lattice atoms per unit volume	Calculated from Eq. (49)
		Material Properties	
C_{11}	246.5 GPa		
C_{12}	147.3 GPa	elastic constants	Kelly and Groves, 1970
C_{44}	75.4 GPa		
b	0.249 nm	Burgers vector	Kelly and Groves, 1970
G	86.0 GPa*	shear modulus	Courtney, 2000
α'	0.3	proportionality constant	

*shear modulus value for isotropic polycrystalline nickel, not single crystal nickel

Table 3. Material properties of copper for comparison with Bassani and Wu (1991) model.

Parameter	Value
τ_0	17.0 MPa
C_{11}	$10\times10^3\tau_0$
C_{12}	$3.8\times10^3\tau_0$
C_{44}	$7.35\times10^3\tau_0$

Table 4. Analytical and numerical applied stresses for initial onset of yielding with single slip.

Orientation, θ	Applied stress, σ_{33}	
	Analytical	*Numerical*
30°	$2.309\tau_0$	$2.312\tau_0$
45°	$2.000\tau_0$	$1.998\tau_0$
60°	$2.309\tau_0$	$2.312\tau_0$

Table 5. Variables for uniaxial tension simulations with nickel single crystals.

Parameter	Value	Definition
	Model calibration parameters	
H_0	125 MPa	hardening parameter
R_0	0	recovery parameter
τ_0	18.3 MPa	initial critical resolved shear stress
H_C	-7.00×10^{6}	coefficient of hydrogen effect on hardening
R_C	0	coefficient of hydrogen effect on recovery
T_C	1.422×10^{6}	coefficient of hydrogen effect on initial critical resolved shear stress
	Hydrogen parameters	
$(c_L)_{initial}$	0.015	lattice hydrogen atoms per lattice atom
$(C_L)_{initial}$	1.27×10^{27} atoms/m^3	lattice hydrogen concentration
$(N_T)_{initial}$	3.255×10^{20} m^{-3}	(total) number of traps per unit volume

10. Figures

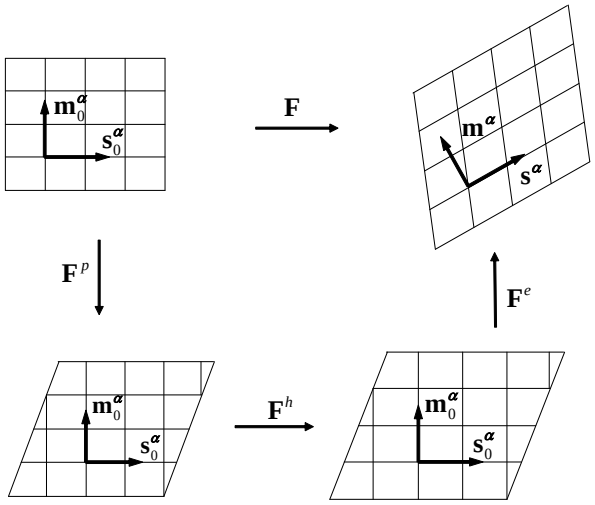

Fig. 1. Schematic representation of the multiplicative decomposition of the deformation gradient, including the dilatational effect of hydrogen.

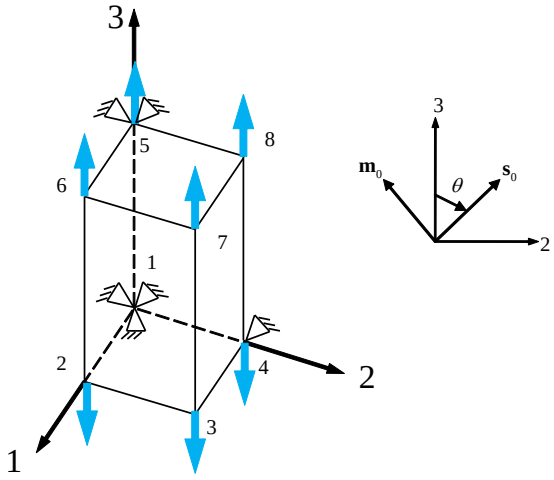

Fig. 2. Loading and boundary conditions for three-dimensional uniaxial tension simulation along with single slip system orientation (in terms of θ).

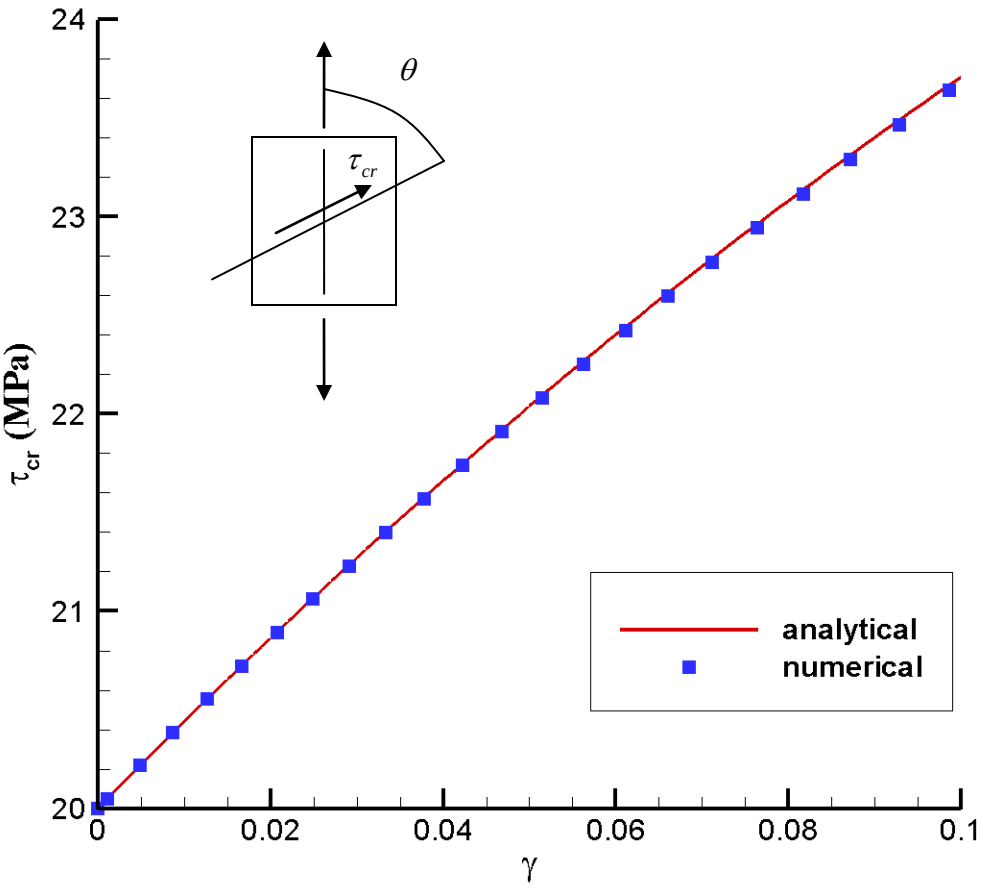

Fig. 3. Plot of critical resolved shear stress, τ_{cr}, versus shear strain, γ, on single active slip system for the test parameters $\tau_0 = 20$ MPa, $H_0 = 125$ MPa, $R_0 = 4$, and $H_c = R_c = 0$. The result shown here is the same for any active slip system in easy glide (for example, if the tensile axis is $[321]$, only slip system #23 becomes active initially). For a more general case, this result is only applicable to the primary slip system in stage I.

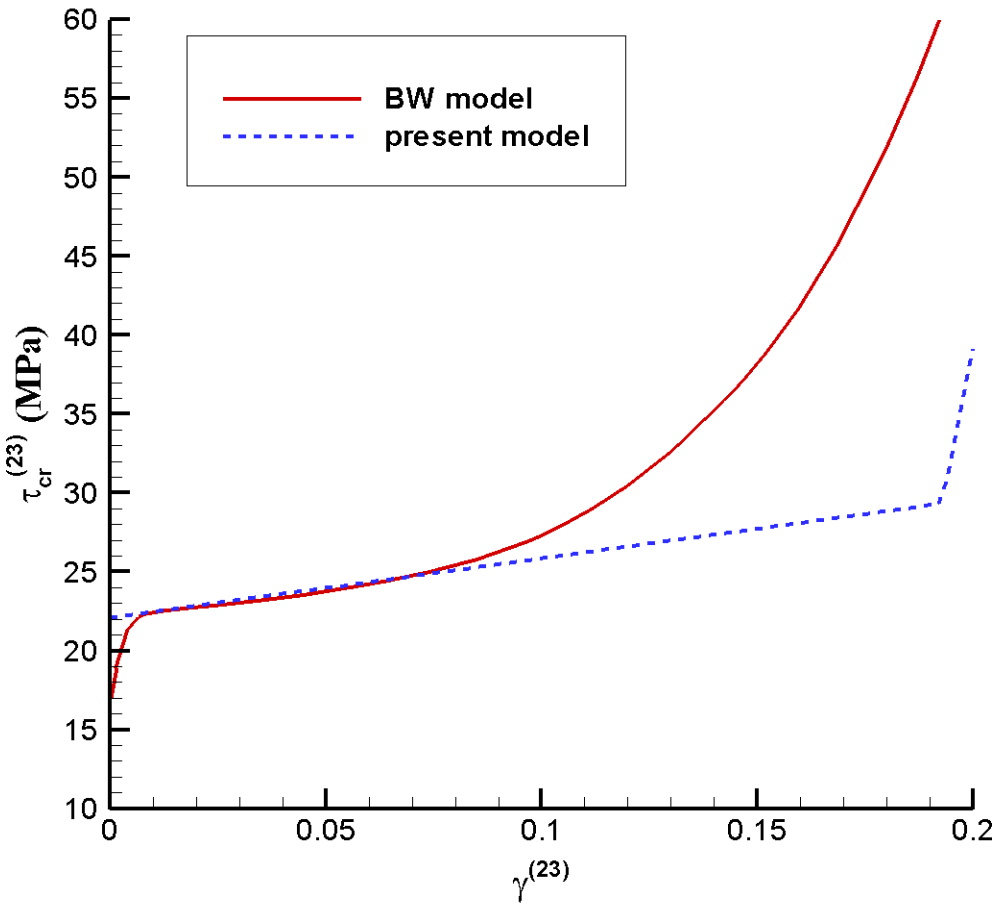

Fig. 4. Comparison of the present model with Bassani and Wu (BW) model. The critical resolved shear stress, $\tau_{cr}^{(23)}$, is plotted versus shear strain, $\gamma^{(23)}$, for tensile axis orientation [321]. Slip system #23 represents the $(\bar{1}\,\bar{1}\,1)[\bar{1}0\,\bar{1}]$ system. The material properties for copper, given in Table 3, are used. The best agreement between the two curves is found using $H_0 = 37.5$ MPa and $F_{II} = 1$. Note that the BW model for single slip includes a high initial rate of hardening, thus the curve for the present model has been offset. The critical resolved shear stress for the present model is increased by 30% to account for this high initial hardening in the BW model.

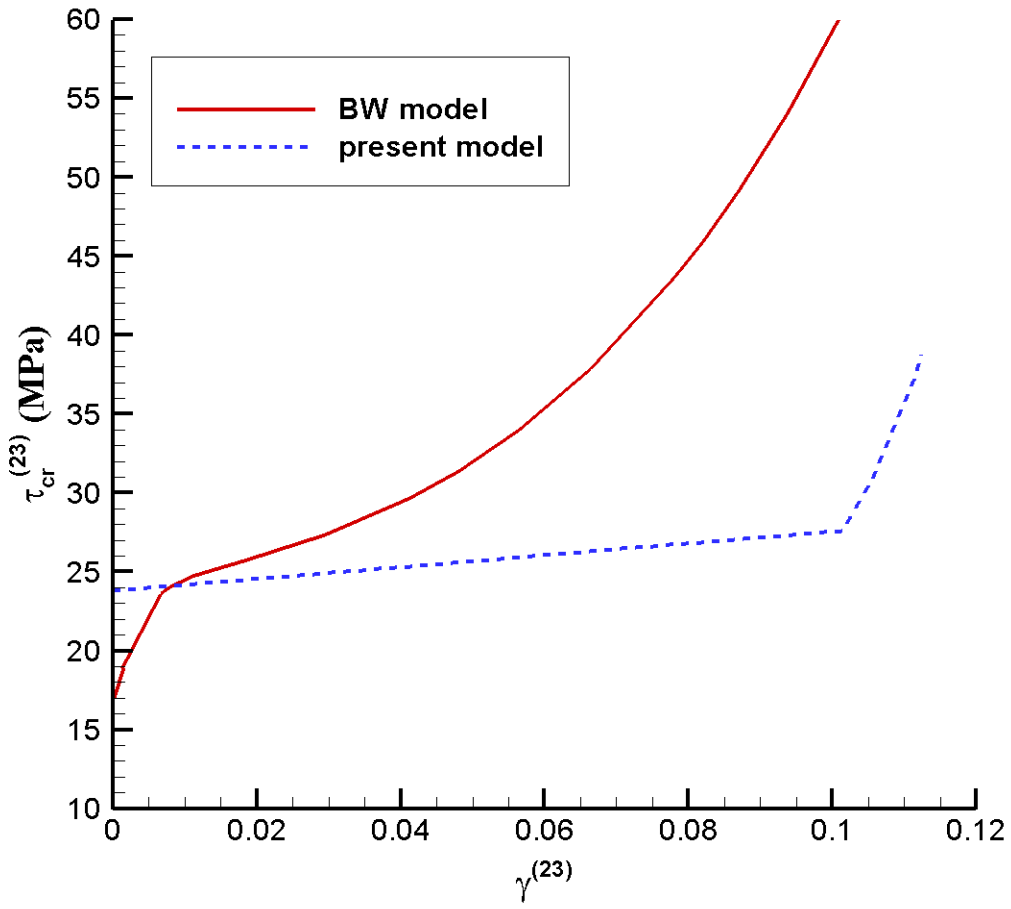

Fig. 5. Comparison of the present model with Bassani and Wu (BW) model. The critical resolved shear stress, $\tau_{cr}^{(23)}$, is plotted versus shear strain, $\gamma^{(23)}$, for tensile axis orientation [632]. Slip system #23 represents the $(\bar{1}\,\bar{1}\,1)[\bar{1}0\,\bar{1}]$ system (see Table 1). The material properties for copper, given in Table 3, are used. The best agreement between the two curves is found using $H_0 = 37.5$ MPa and $F_{II} = 1$. Note that the BW model for single slip includes a high initial rate of hardening, , thus the curve for the present model has been offset. The critical resolved shear stress for the present model is increased by 40% to account for this high initial hardening in the BW model.

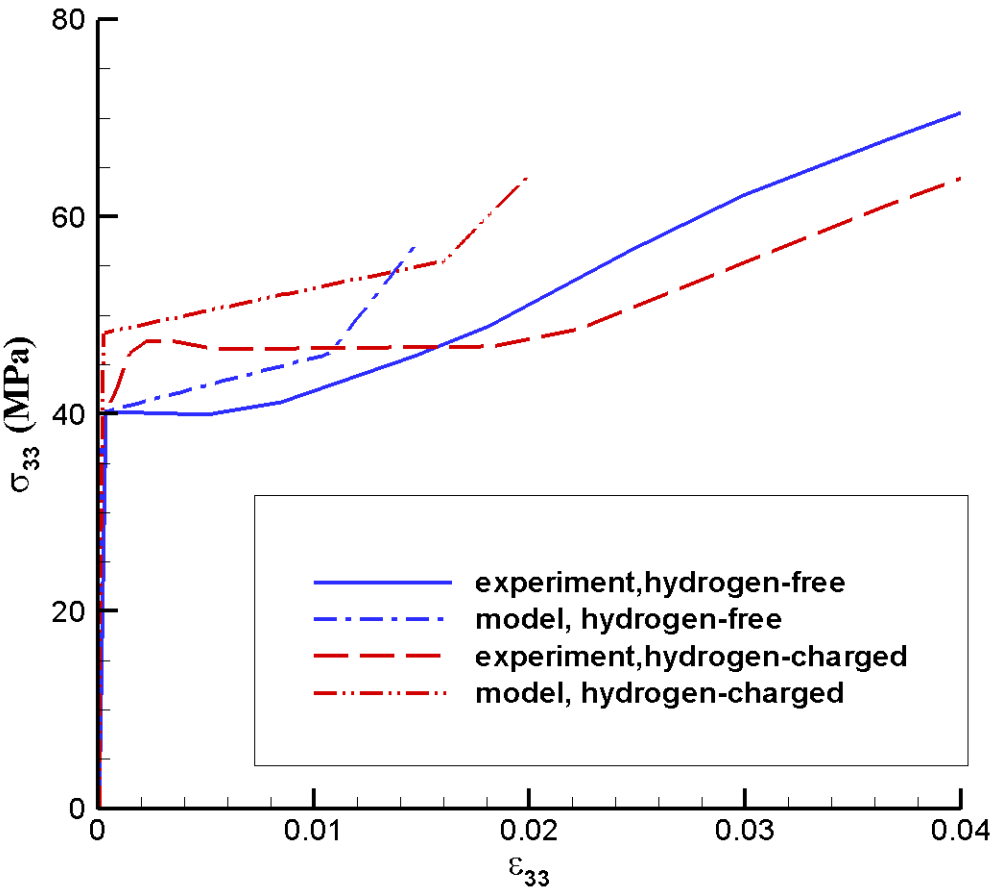

Fig. 6. Stress-strain curves predicted by the model along with experimental data from Yagodzinskyy et al. (2009). The tensile axis of the nickel single crystal are aligned with the $[\bar{1}67]$-direction in both the model and the experimental case. The parameters used for the model predictions are found in Table 5. For better agreement with the experimental stress-strain curves, the stage II parameter, F_{II}, in the model is set to 0.5.

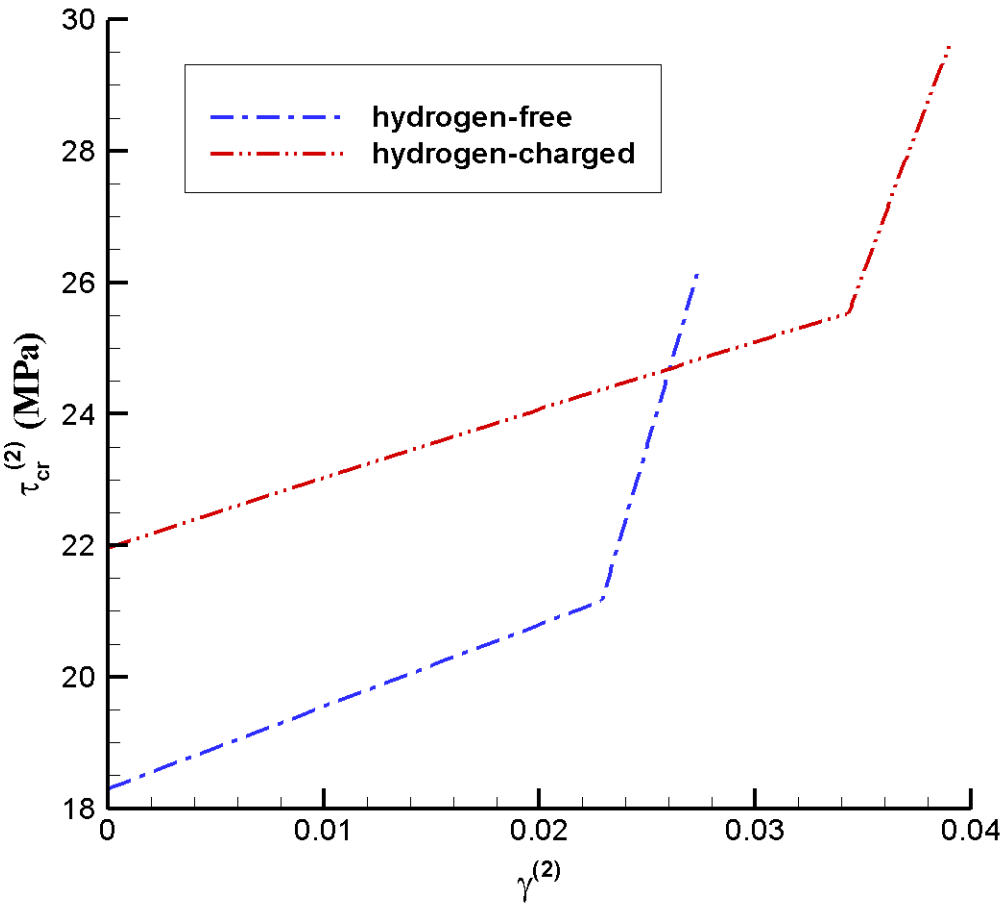

Fig. 7. Critical resolved shear stress versus shear strain on $(111)[\bar{1}01]$ (slip system #2). The tensile axis of the nickel single crystal is aligned with the $[\bar{1}67]$-direction. The parameters used are found in Table 5. The stage II parameter, F_{II}, was set to 0.5.

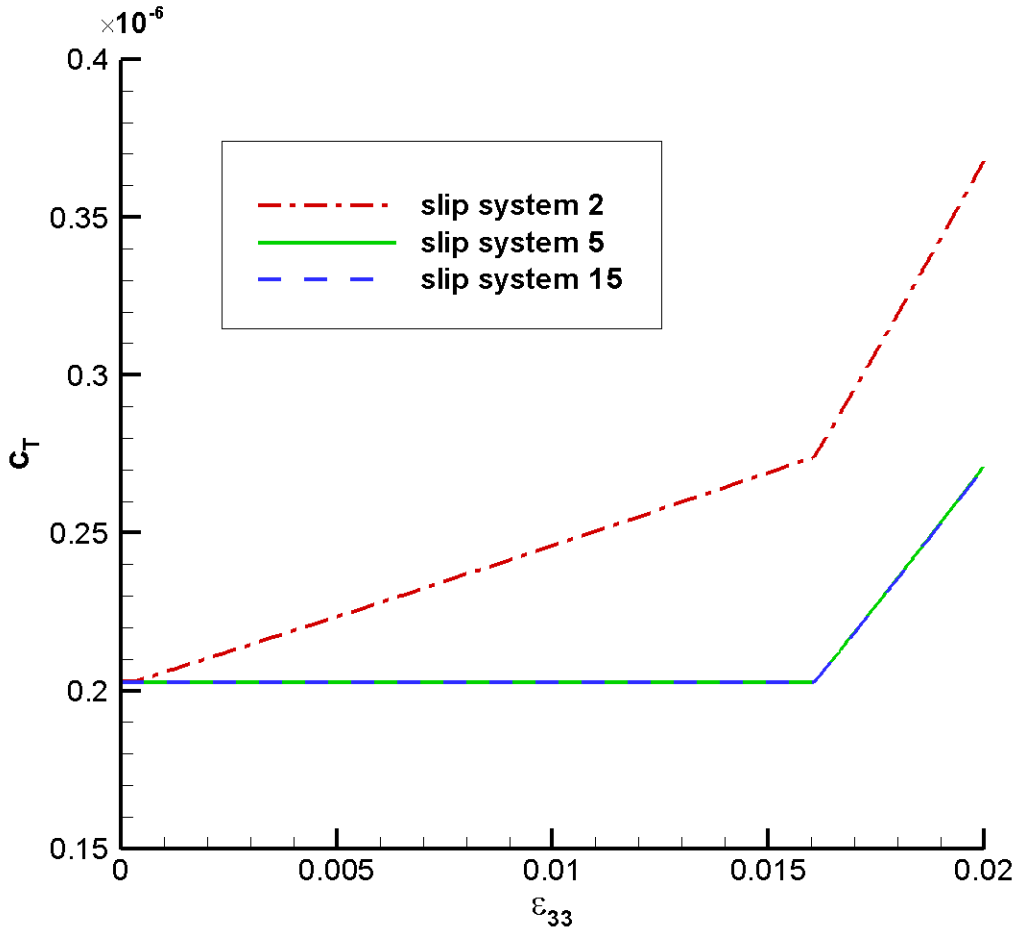

Fig. 8. Trapped hydrogen atoms per lattice atom, c_T, plotted versus axial strain, ε_{33}, for the three slip systems activated over the course of the simulation. The $(111)[\bar{1}01]$ system (slip system #2) is initially active in stage I, and the $(1\bar{1}\bar{1})[\bar{1}0\bar{1}]$ and $(111)[\bar{1}10]$ systems (slip systems #5 and #15, respectively) become active in stage II. Since the secondary slip systems do not become active until a strain of about 0.16, the change in hydrogen presence on these systems is negligible and thus the curves for these systems appear flat. The tensile axis of the nickel single crystal is aligned with the $[\bar{1}67]$-direction. The parameters used are found in Table 5. The stage II parameter, F_{II}, is set to 0.5.

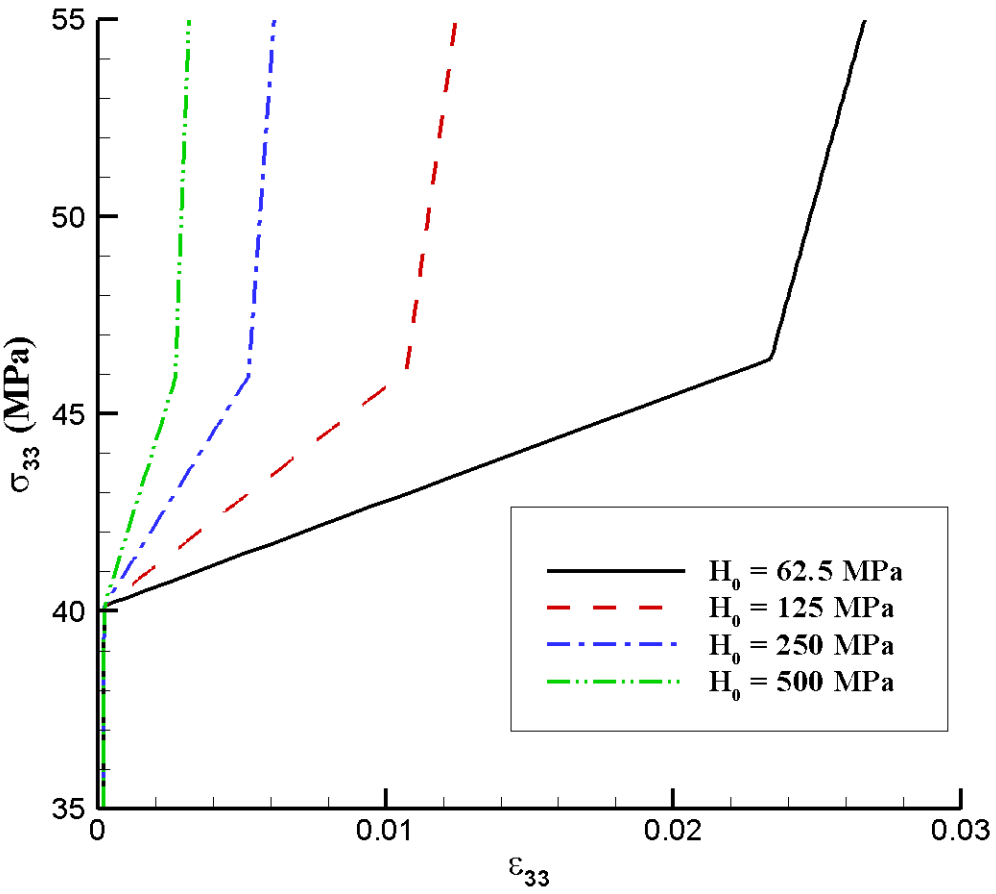

Fig. 9. Stress-strain curves for various values of hardening parameter, H_0, in the absence of hydrogen. The tensile axis of the nickel single crystal is aligned with the $[\bar{1}67]$-direction. For this simulation, $\tau_0 = 18.3$ MPa, $R_0 = 0$, and $F_{II} = 1$. The coefficients H_C and R_C are irrelevant since the trapped hydrogen concentration is zero.

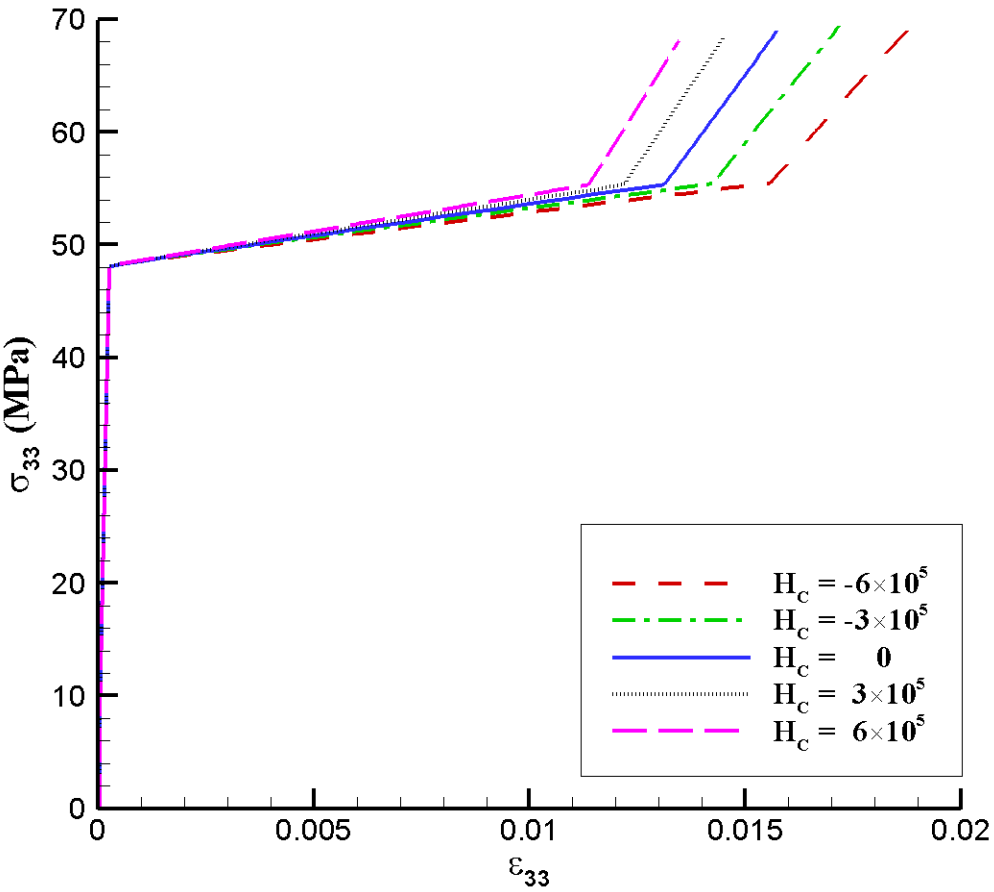

Fig. 10. Stress-strain curves for various values of the coefficient of the hydrogen effect on hardening, H_C, in nickel. The tensile axis of the nickel single crystal is aligned with the $[\bar{1}67]$-direction. For these simulations, the following parameters are held constant: $\tau_0 = 18.3$ MPa, $T_C = 1.422 \times 10^6$, $H_0 = 125$ MPa, $R_0 = 0$, $R_C = 0$, and $F_{II} = 1.0$.

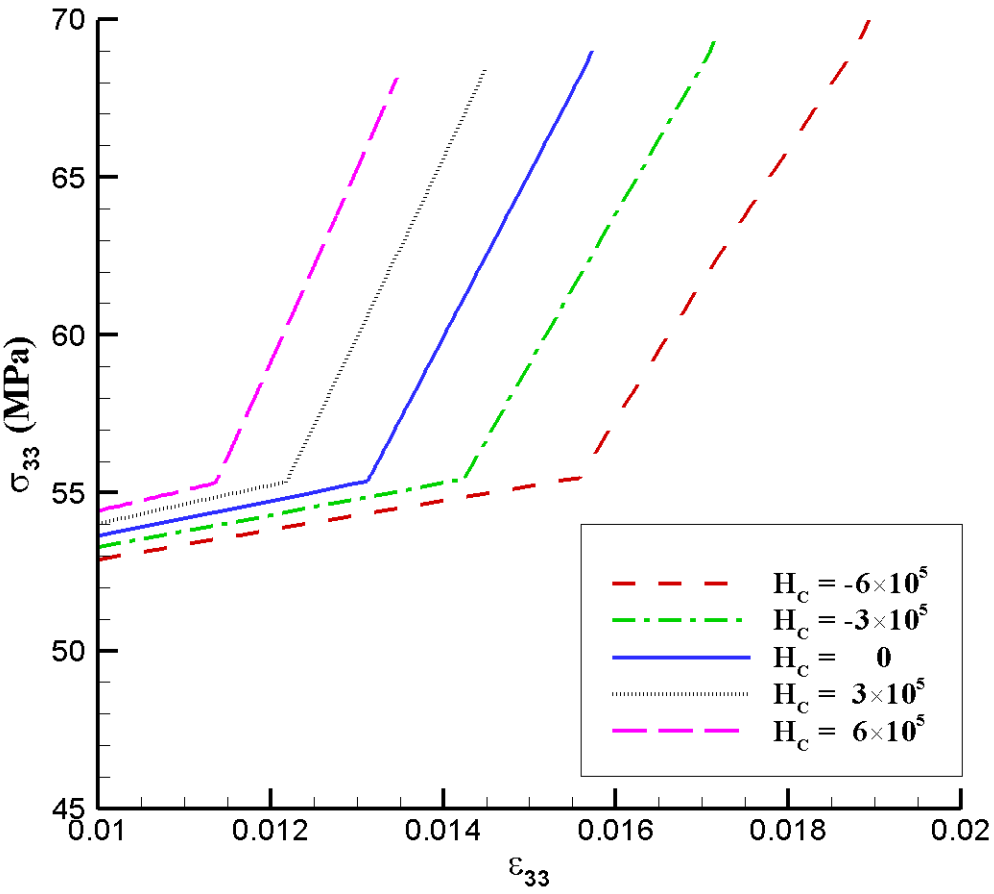

Fig. 11. Magnified view of stress-strain curves for various values of H_C (shown in Fig. 10) near the transition points from stage I to stage II. For these simulations, the following parameters are held constant: $\tau_0 = 18.3$ MPa, $T_C = 1.422 \times 10^6$, $H_0 = 125$ MPa, $R_0 = 0$, $R_C = 0$, and $F_{II} = 1.0$.

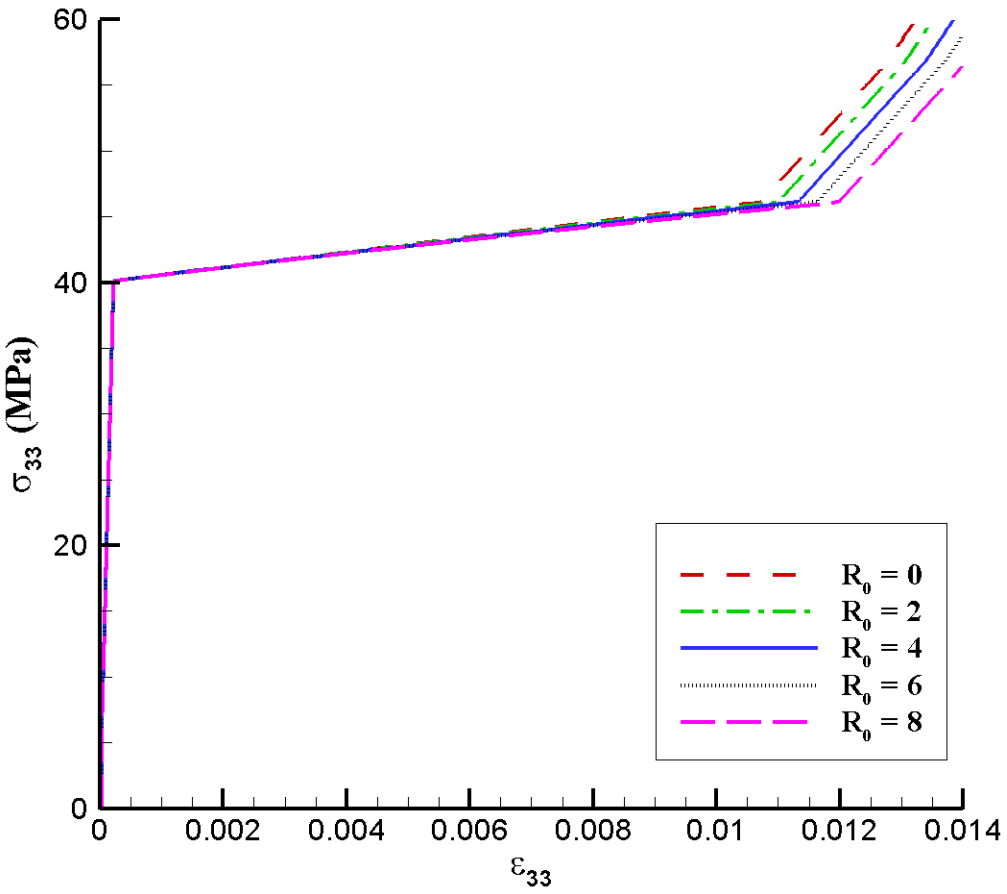

Fig. 12. Stress-strain curves for various values of the recovery parameter, R_0, in the absence of hydrogen. The tensile axis of the nickel single crystal is aligned with the $[\bar{1}67]$-direction. For this simulation, $\tau_0 = 18.3$ MPa, $H_0 = 125$ MPa, and $F_{II} = 1$.

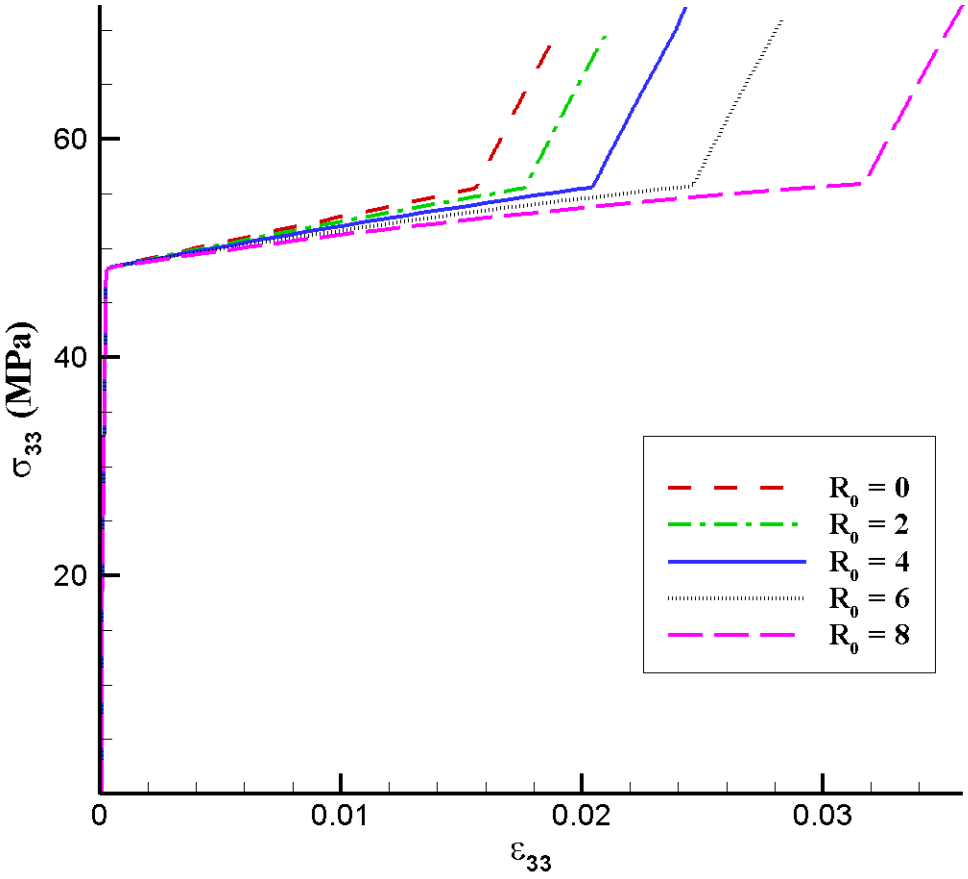

Fig. 13. Stress-strain curves for varying values of the recovery parameter, R_0, for the hydrogen-charged specimen. The tensile axis of the nickel single crystal is aligned with the $[\bar{1}67]$-direction. For this simulation, the following parameters are held constant: $\tau_0 = 18.3$ MPa, $H_0 = 125$ MPa, $H_C = -7.0\times10^5$, $R_C = 0$, and $F_{II} = 1$.

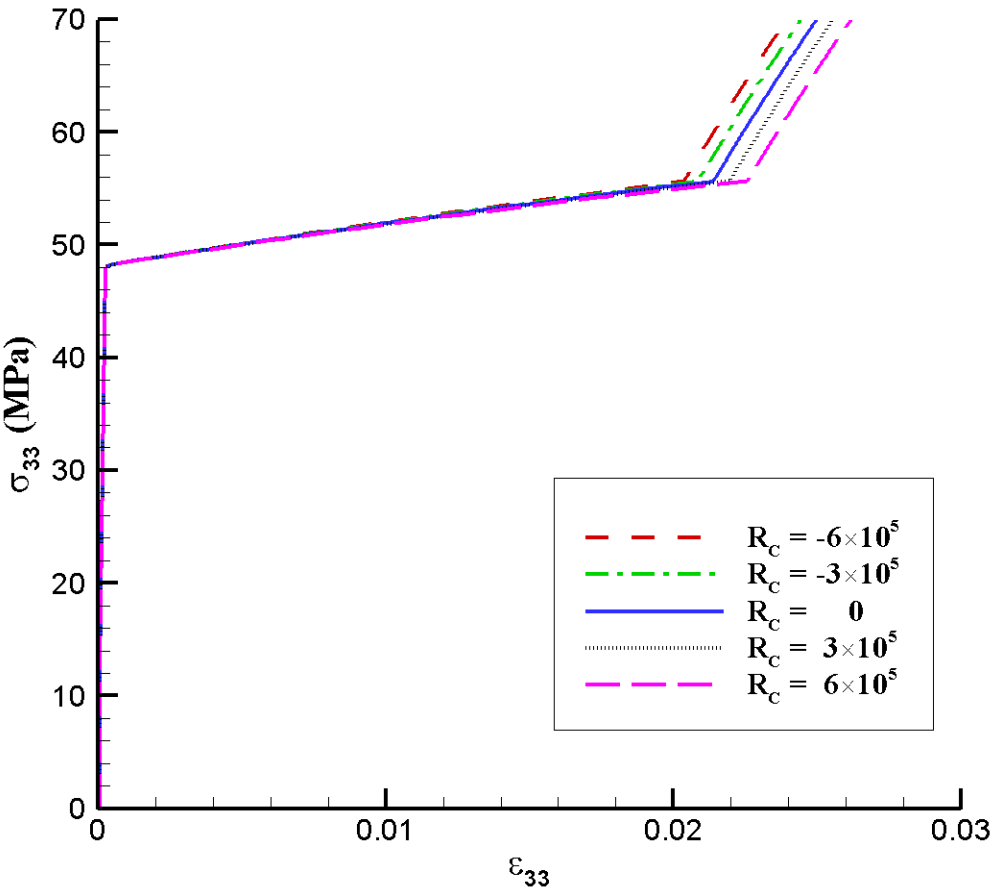

Fig. 14. Stress-strain curves for varying values of the coefficient of the hydrogen effect on recovery, R_C, in the hydrogen-charged specimen. The tensile axis of the nickel single crystal is aligned with the $[\bar{1}67]$-direction. For this simulation, the following parameters are held constant: $\tau_0 = 18.3$ MPa, $H_0 = 125$ MPa, $H_C = -7.0\times10^5$, $R_0 = 4$, and $F_{II} = 1$.

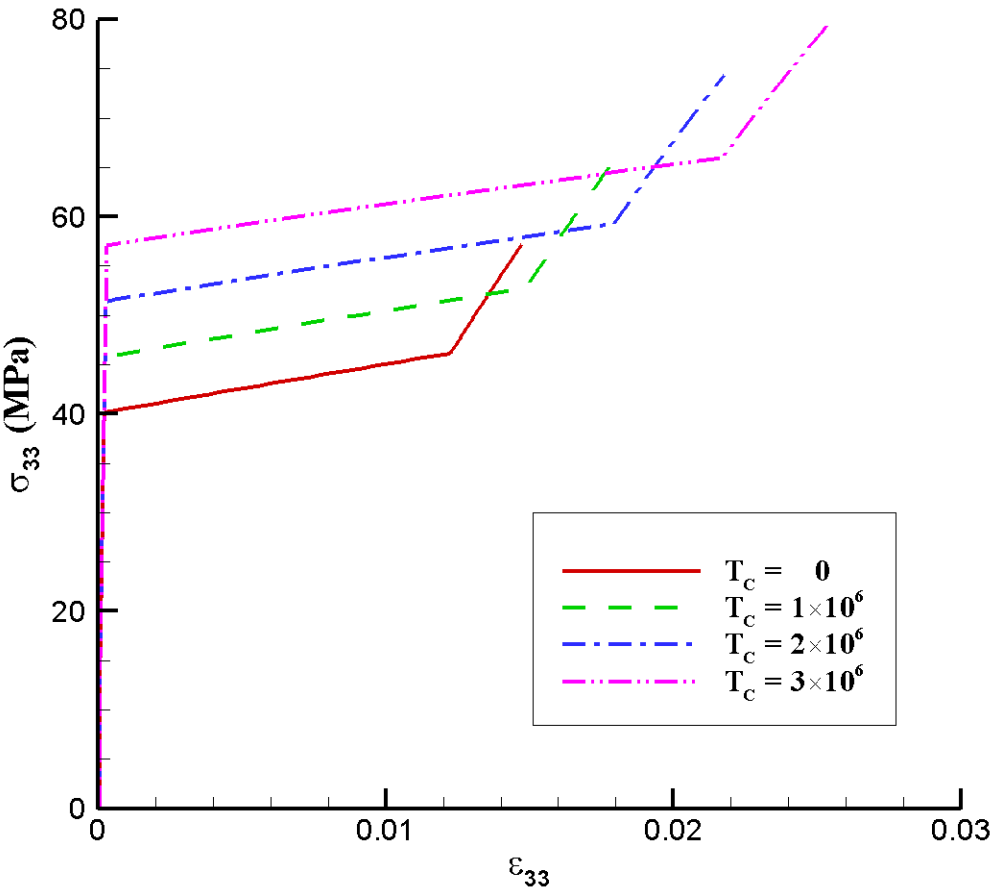

Fig. 15. Stress-strain curves for varying values of the coefficient of the hydrogen effect on the initial critical resolved shear stress, T_C, in the hydrogen-charged specimen. The tensile axis of the nickel single crystal is aligned with the $[\bar{1}67]$-direction. For this simulation, the following parameters are held constant: $\tau_0 = 18.3$ MPa, $H_0 = 125$ MPa, $H_C = -7.0\times10^5$, $R_0 = 0$, $R_C = 0$, and $F_{II} = 1$.

Appendix A: Numerical Integration of Constitutive Equations

A displacement-based finite element formulation is used to numerically integrate the constitutive equation outlined in Section 3. In performing this integration at each Gauss points, the set $\left(\boldsymbol{\Sigma}_n, \gamma_n^{\delta}, \mathbf{F}_n^p, \mathbf{F}_n, (C_L)_n\right)$ at time t_n as well as the deformation gradient $\mathbf{F}_{n+1}$ at t_{n+1} are known, and the set $\left(\boldsymbol{\Sigma}_{n+1}, \gamma_{n+1}^{\delta}, \mathbf{F}_{n+1}^p, (C_L)_{n+1}\right)$ is to be determined.

Integration of Eq. (34) (Aravas 1994) gives

$$\mathbf{F}_{n+1}^p = \exp\left(\sum_{\delta} \Delta\gamma^{\delta} \mathbf{s}_0^{\delta} \mathbf{m}_0^{\delta}\right) \cdot \mathbf{F}_n^p, \tag{A.1}$$

which can be inverted to give

$$\begin{aligned} \mathbf{F}_{n+1}^{p\,-1} &= \mathbf{F}_n^{p\,-1} \cdot \exp\left(-\sum_{\delta} \Delta\gamma^{\delta} \mathbf{s}_0^{\delta} \mathbf{m}_0^{\delta}\right) \\ &= \mathbf{F}_n^{p\,-1} \cdot \exp\left(-\mathbf{G}\right) = \mathbf{F}_n^{p\,-1} \cdot \left(\mathbf{I} - \mathbf{G} + \tfrac{1}{2}\mathbf{G}\cdot\mathbf{G} + O(\Delta\gamma^3)\right), \end{aligned} \tag{A.2}$$

where

$$\mathbf{G} = \sum_{\delta} \Delta\gamma^{\delta} \mathbf{s}_0^{\delta} \mathbf{m}_0^{\delta}\,. \tag{A.3}$$

Eq. (11) is inverted to express the elastic part of the deformation gradient as

$$\mathbf{F}_{n+1}^e = \mathbf{F}_{n+1} \cdot \mathbf{F}_{n+1}^{p\,-1} \cdot \mathbf{F}_{n+1}^{h\,-1}\,. \tag{A.4}$$

Based on the treatment of the total hydrogen concentration addressed in Subsection 3.2, the current concentration and initial concentrations of hydrogen are equal, and Eq. (14) is used to show that the hydrogen part of the deformation gradient, $\mathbf{F}^h$, will equal the identity tensor, $\mathbf{I}$. Eq. (A.4) can now be written as

$$\mathbf{F}_{n+1}^e = \mathbf{F}_{n+1} \cdot \mathbf{F}_{n+1}^{p\,-1}\,. \tag{A.5}$$

Substituting Eq. (A.2) into Eq. (A.5) yields

$$\begin{aligned} \mathbf{F}_{n+1}^e &= \mathbf{F}_{n+1} \cdot \mathbf{F}_{n+1}^{p\,-1} \cdot \mathbf{F}_{n+1}^{h\,-1} = \mathbf{F}_{n+1} \cdot \mathbf{F}_n^{p\,-1} \cdot \left(\mathbf{I} - \mathbf{G} + \tfrac{1}{2}\mathbf{G}\cdot\mathbf{G} + O(\Delta\gamma^3)\right) \cdot \mathbf{I} \\ &= \mathbf{F}_{trial} \cdot \left(\mathbf{I} - \mathbf{G} + \tfrac{1}{2}\mathbf{G}\cdot\mathbf{G} + O(\Delta\gamma^3)\right), \end{aligned} \tag{A.6}$$

where

$$\mathbf{F}_{trial} = \mathbf{F}_{n+1} \cdot \mathbf{F}_n^{p\,-1}\,. \tag{A.7}$$

The plastic part of the deformation gradient for the next step is calculated as

$$\mathbf{F}^{p}_{n+1} = \mathbf{F}_{n+1} \cdot \mathbf{F}^{e\,-1}_{n+1}. \tag{A.8}$$

The Cauchy-Green deformation tensor and the Green strain tensor due to elastic deformation at step $n+1$ are written as

$$\mathbf{C}^{e}_{n+1} = \mathbf{F}^{e\,T}_{n+1} \cdot \mathbf{F}^{e}_{n+1} \tag{A.9}$$

and

$$\mathbf{E}^{e}_{n+1} = \tfrac{1}{2}(\mathbf{C}^{e}_{n+1} - \mathbf{I}). \tag{A.10}$$

The second Piola-Kirchhoff stress is expressed in the intermediate configuration as

$$\mathbf{S}^{e}_{n+1} = \underset{\sim}{\mathbf{C}} : \mathbf{E}^{e}_{n+1}. \tag{A.11}$$

The stress tensor $\mathbf{\Sigma}_{n+1}$ is calculated as in Eq. (38):

$$\mathbf{\Sigma}_{n+1} = \mathbf{S}^{e}_{n+1} \cdot \mathbf{C}^{e}_{n+1}. \tag{A.12}$$

To complete the integration, it is necessary to evaluate the trapped hydrogen concentration $(C_T^{\delta})_{n+1}$, critical resolved shear stress $(\tau_{cr}^{\delta})_{n+1}$, and trap density $(N_T^{\delta})_{n+1}$, all at time t_{n+1}. This is done using the known values for $(C_T^{\delta})_n$, $(\tau_{cr}^{\delta})_n$, and $(N_T^{\delta})_n$ at time t_n, as well as the lattice hydrogen concentration $(C_L)_{n+1}$ and the shear strains γ^{δ}_{n+1} at time t_{n+1}.

The trapped hydrogen concentration can be found in terms of the lattice concentration at $n+1$ and the number of traps per unit volume at $n+1$ through Eq. (46) along with the hydrogen concentration definitions given in Eqs. (48) and (50):

$$(C_T^{\delta})_{n+1} = \frac{K_T \alpha (N_T^{\delta})_{n+1}}{\beta N_L + (K_T - 1)(C_L)_{n+1}} (C_L)_{n+1}. \tag{A.13}$$

A backward Euler integration is applied to the critical resolved shear stress evolution equation (see Eq. (64)). For simplicity in the following presentation, the piecewise term associated with stage II in this equation is left out of the following calculations. This term is dealt with at the transition point between stage I and stage II and does not change the integration method for the evolution equation. After applying the integration scheme, the critical resolved shear stress at step $n+1$ is given by

$$(\tau_{cr}^{\delta})_{n+1} = \frac{\left(H^{\delta}_{n+1} + R^{\delta}_{n+1}\tau_0\right)\Delta\gamma^{\delta} + \left(\tau_{cr}^{\delta}\right)_n}{1 + R^{\delta}_{n+1}\Delta\gamma^{\delta}}, \tag{A.14}$$

where H_{n+1}^{δ} and R_{n+1}^{δ} are evaluated using Eqs. (65) and (66), respectively. The trap density at step $n+1$, which is expressed in terms of the dislocation density in Eq. (53), can now be given in terms of the critical resolved shear stress at step $n+1$ by applying the fundamental relationship given by Eq. (2):

$$(N_T^{\delta})_{n+1} = \left(\frac{(\tau_{cr}^{\delta})_{n+1}}{\alpha' \mu} \right)^2 \frac{1}{b^3}. \tag{A.15}$$

The set of equations given by Eqs. (A.13)-(A.15) is solved for $(C_T^{\delta})_{n+1}$, $(\tau_{cr}^{\delta})_{n+1}$, and $(N_T^{\delta})_{n+1}$, at each step using the method outlined in Appendix B.

The values of the $\Delta\gamma^{\delta}$s and $(C_L)_{n+1}$ are determined based on the yield condition on each active slip system and the hydrogen balance equation. The first set of conditions is the yield condition, given by Eq. (61), which can be written for step $n+1$ as

$$f^{\delta} = \mathbf{m}_0^{\delta} \cdot \boldsymbol{\Sigma}_{n+1} \cdot \mathbf{s}_0^{\delta} - (\tau_{cr}^{\delta})_{n+1} = 0. \tag{A.16}$$

The second condition is the hydrogen balance equation given in Eq. (55), which can be written for step $n+1$ as

$$h = (C_L)_{n+1} + \sum_{\delta} (C_T^{\delta})_{n+1} - C_0 = 0. \tag{A.17}$$

The system of equations represented by (A.16)-(A.17) is solved iteratively by using Newton's method. The evaluation of these conditions is dependent on the $\Delta\gamma^{\delta}$s and $(C_L)_{n+1}$ as they are necessary to calculate $\boldsymbol{\Sigma}_{n+1}$, $(\tau_{cr}^{\delta})_{n+1}$, and $(C_T^{\delta})_{n+1}$, as described earlier in this appendix. The process is initiated using the set $\left(\boldsymbol{\Sigma}_n, \gamma_n^{\delta}, \mathbf{F}_n^p, \mathbf{F}_n, (C_L)_n\right)$ at step n.

Having obtained the solution at t_{n+1}, the Cauchy stress $\boldsymbol{\sigma}_{n+1}$ can be calculated from $\boldsymbol{\Sigma}_{n+1}$ using Eq. (36) and the definition of the Kirchhoff stress:

$$\boldsymbol{\sigma}_{n+1} = J\boldsymbol{\tau}_{n+1} = J\mathbf{F}_{n+1}^e \cdot \boldsymbol{\Sigma}_{n+1} \cdot \mathbf{F}_{n+1}^{e\,-1}. \tag{A.18}$$

J can be written as

$$J = \det(\mathbf{F}_{n+1}) = \det(\mathbf{F}_{n+1}^e \cdot \mathbf{F}_{n+1}^h \cdot \mathbf{F}_{n+1}^p) = \det(\mathbf{F}_{n+1}^e)\det(\mathbf{F}_{n+1}^h)\det(\mathbf{F}_{n+1}^p). \tag{A.19}$$

Since $\mathbf{F}_{n+1}^h = \mathbf{I}$ and the plastic deformation is isochoric, $\det(\mathbf{F}_{n+1}^h)$ and $\det(\mathbf{F}_{n+1}^p)$ both equal unity, and Eq. (A.19) reduces to

$$J = \det(\mathbf{F}_{n+1}^e), \tag{A.20}$$

so $\boldsymbol{\sigma}_{n+1}$ can be written as

$$\boldsymbol{\sigma}_{n+1} = \det(\mathbf{F}^{e}_{n+1})\mathbf{F}^{e}_{n+1} \cdot \boldsymbol{\Sigma}_{n+1} \cdot \mathbf{F}^{e\,-1}_{n+1}. \tag{A.21}$$

The Cauchy stress $\boldsymbol{\sigma}_{n+1}$ and the approximation of the elastoplastic tangent modulus (see Appendix C) are used by Abaqus in the global equilibrium iteration.

Appendix B: Evaluation of the Critical Resolved Shear Stress, Trapped Hydrogen Concentration, and Trap Density

Due to the interdependency of the critical resolved shear stress, the hydrogen concentration, and the trap density, a method is required that will solve the system of Eqs. (A.13)-(A.15) governing these parameters. Upon each iteration used in determining $(\gamma^{\delta})_{n+1}$ and $(C_L)_{n+1}$ (see Appendix A), the system of equations must be solved for each active slip system. The set $\left((C_T^{\delta})_n, (\tau_{cr}^{\delta})_n, (N_T^{\delta})_n\right)$ at time t_n as well as the assumed values $(\gamma^{\delta})_{n+1}$ and $(C_L)_{n+1}$ at t_{n+1} are known (see Appendix A), and the set $\left((C_T^{\delta})_{n+1}, (\tau_{cr}^{\delta})_{n+1}, (N_T^{\delta})_{n+1}\right)$ is to be determined. It is noted that this system needs to be solved for each active slip system.

The system of equations is restated below:

$$(C_T^{\delta})_{n+1} = \frac{K_T \alpha (N_T^{\delta})_{n+1}}{\beta N_L + (K_T - 1)(C_L)_{n+1}} (C_L)_{n+1}, \tag{B.1}$$

$$(\tau_{cr}^{\delta})_{n+1} = \frac{\left(H_{n+1}^{\delta} + R_{n+1}^{\delta}\tau_0\right)\Delta\gamma^{\delta} + \left(\tau_{cr}^{\delta}\right)_n}{1 + R_{n+1}^{\delta}\Delta\gamma^{\delta}}, \tag{B.2}$$

and

$$(N_T^{\delta})_{n+1} = \left(\frac{(\tau_{cr}^{\delta})_{n+1}}{\alpha'\mu}\right)^2 \frac{1}{b^3}. \tag{B.3}$$

This is a system of three nonlinear equations with three unknowns, and it can readily be solved using Newton's method. It should be noted that H_{n+1}^{δ} and R_{n+1}^{δ} are functions of $(C_T^{\delta})_{n+1}$. The system of linear equations to be solved for each slip system is given as follows (the superscript is dropped here since all parameters are from slip system δ):

$$\begin{bmatrix} \frac{\partial f_1}{\partial \Delta C_T} & \frac{\partial f_1}{\partial \Delta \tau_{cr}} & \frac{\partial f_1}{\partial \Delta N_T} \\ \frac{\partial f_2}{\partial \Delta C_T} & \frac{\partial f_2}{\partial \Delta \tau_{cr}} & \frac{\partial f_2}{\partial \Delta N_T} \\ \frac{\partial f_2}{\partial \Delta C_T} & \frac{\partial f_2}{\partial \Delta \tau_{cr}} & \frac{\partial f_2}{\partial \Delta N_T} \end{bmatrix} \begin{Bmatrix} d\Delta C_T \\ d\Delta \tau_{cr} \\ d\Delta N_T \end{Bmatrix} = -\begin{Bmatrix} f_1 \\ f_2 \\ f_3 \end{Bmatrix}, \tag{B.4}$$

where

$$f_1 = (C_T)_{n+1} - \frac{K_T \alpha (C_L)_{n+1}}{\beta N_L + (K_T - 1)(C_L)_{n+1}} (N_T)_{n+1},$$

$$f_2 = (\tau_{cr})_{n+1} - \frac{\left[H_{n+1} + R_{n+1}\tau_0\right]\Delta\gamma + \left(\tau_{cr}\right)_n}{1 + R_{n+1}\Delta\gamma},$$

$$f_3 = (N_T)_{n+1} - \left(\frac{(\tau_{cr})_{n+1}}{\alpha' \mu}\right)^2 \frac{1}{b^3},$$

$$\frac{f_1}{\partial \Delta C_T} = 1, \quad \frac{\partial f_1}{\partial \Delta N_T} = -\frac{K_T \alpha (C_L)_{n+1}}{\beta N_L + (K_T - 1)\Delta\gamma}, \quad \frac{\partial f_1}{\partial \Delta \tau_{cr}} = 0,$$

$$\frac{\partial f_2}{\partial \Delta C_T} = -\frac{\partial (\tau_{cr})_{n+1}}{\partial \Delta C_T}, \quad \frac{\partial f_2}{\partial \Delta \tau_{cr}} = 1, \quad \frac{\partial f_2}{\partial \Delta N_T} = 0,$$

$$\frac{\partial f_3}{\partial \Delta C_T} = 0, \quad \frac{\partial f_3}{\partial \Delta \tau_{cr}} = -\frac{2(\tau_{cr})_{n+1}}{(\alpha' \mu)^2} \frac{1}{b^3}, \quad \frac{\partial f_3}{\partial \Delta N_T} = 1,$$

and

$$\frac{\partial (\tau_{cr})_{n+1}}{\partial \Delta C_T} = \frac{\partial}{\partial \Delta C_T} \left\{ \frac{\left[H_{n+1} + R_{n+1}\tau_0\right]\Delta\gamma + \left(\tau_{cr}\right)_n}{1 + R_{n+1}\Delta\gamma} \right\}$$

$$= \frac{\Delta\gamma}{1 + R_{n+1}\Delta\gamma} \frac{\partial}{\partial \Delta C_T} \left[H_{n+1} + R_{n+1}\tau_0\right] - \frac{\left[H_{n+1} + R_{n+1}\tau_0\right]\Delta\gamma + \left(\tau_{cr}\right)_n}{\left[1 + R_{n+1}\Delta\gamma\right]^2} \Delta\gamma \frac{\partial R_{n+1}}{\partial \Delta C_T}$$

$$= \frac{\Delta\gamma}{\left[1 + R_{n+1}\Delta\gamma\right]^2} \left\{ \left[1 + R_{n+1}\Delta\gamma\right] \left[\frac{\partial H_{n+1}}{\partial \Delta C_T} + \frac{\partial R_{n+1}}{\partial \Delta C_T} \tau_0 \right] \right.$$

$$\left. - \left[\left(H_{n+1} + R_{n+1}\tau_0\right)\Delta\gamma_{n+1} + \left(\tau_{cr}\right)_n \right] \frac{\partial R_{n+1}}{\partial \Delta C_T} \right\}.$$

The set $\left((C_T)_n, (\tau_{cr})_n, (N_T)_n\right)$ at step n (on a given slip system) is used to initiate the iterative process.

Appendix C: Consistent Elastoplastic Tangent Modulus

To solve the incremental constitutive equations of the elastoplastic boundary value problem in the presence of hydrogen, the consistent elastoplastic tangent modulus (Jacobian) needs to be obtained and implemented in Abaqus. The consistent elastoplastic tangent modulus, $\underset{\sim}{\mathbf{C}}^c$, is defined as

$$\underset{\sim}{\mathbf{C}}^c = \left(\frac{\partial \Delta \boldsymbol{\tau}}{\partial \Delta \mathbf{E}} \right)_{t_n + \Delta t}, \tag{C.1}$$

where $\Delta \boldsymbol{\tau}$ is increment of the Kirchhoff stress over the time interval $(t_n, t_n + \Delta t)$ and $\Delta \mathbf{E}$ is the corresponding strain increment such that $\dot{\mathbf{E}} = \mathbf{F}^{eT} \cdot \mathbf{D} \cdot \mathbf{F}^e$. $\underset{\sim}{\mathbf{C}}^c$ is calculated at time $t_{n+1} = t_n + \Delta t$ since the equilibrium equations are satisfied at t_{n+1} for an implicit finite element scheme.

An approximation to $\underset{\sim}{\mathbf{C}}^c$ can be obtained by expressing the Jaumann rate of the Kirchhoff stress, $\overset{\nabla}{\boldsymbol{\tau}}$, in terms of the deformation rate, $\mathbf{D}$ as

$$\overset{\nabla}{\boldsymbol{\tau}} = \underset{\sim}{\mathbf{L}}_J : \mathbf{D}, \tag{C.2}$$

where $\underset{\sim}{\mathbf{L}}_J$ is the approximation to the tangent modulus, the derivation of which is presented in this appendix.

The time derivative of Eq. (37) yields

$$\dot{\boldsymbol{\tau}} = \tfrac{d}{dt}\left(\mathbf{F}^e \cdot \mathbf{S}^e \cdot \mathbf{F}^{eT} \right) = \dot{\mathbf{F}}^e \cdot \mathbf{S}^e \cdot \mathbf{F}^{eT} + \mathbf{F}^e \cdot \dot{\mathbf{S}}^e \cdot \mathbf{F}^{eT} + \mathbf{F}^e \cdot \mathbf{S}^e \cdot \dot{\mathbf{F}}^{eT}. \tag{C.3}$$

The relations in Eqs. (17) and (45) are substituted into the Eq. (C.3) to give

$$\dot{\boldsymbol{\tau}} = \mathbf{L}^e \cdot \mathbf{F}^e \cdot \mathbf{S}^e \cdot \mathbf{F}^{eT} + \mathbf{F}^e \cdot [\underset{\sim}{\mathbf{C}} : \dot{\mathbf{E}}^e] \cdot \mathbf{F}^{eT} + \mathbf{F}^e \cdot \mathbf{S}^e \cdot \mathbf{F}^{eT} \cdot \mathbf{L}^{eT}. \tag{C.4}$$

Applying Eqs. (37) and (40), the Eq. (C.4) can be written as

$$\dot{\boldsymbol{\tau}} = \mathbf{L}^e \cdot \boldsymbol{\tau} + \mathbf{F}^e \cdot [\underset{\sim}{\mathbf{C}} : (\mathbf{F}^{eT} \cdot \mathbf{D}^e \cdot \mathbf{F}^e)] \cdot \mathbf{F}^{eT} + \boldsymbol{\tau} \cdot \mathbf{L}^{eT}. \tag{C.5}$$

Decomposing $\mathbf{L}^e$ into symmetric and antisymmetric parts, Eq. (C.5) is written as

$$\begin{aligned} \dot{\boldsymbol{\tau}} &= (\mathbf{D}^e + \mathbf{W}^e) \cdot \boldsymbol{\tau} + \mathbf{F}^e \cdot [\underset{\sim}{\mathbf{C}} : (\mathbf{F}^{eT} \cdot \mathbf{D}^e \cdot \mathbf{F}^e)] \cdot \mathbf{F}^{eT} + \boldsymbol{\tau} \cdot (\mathbf{D}^e + \mathbf{W}^e)^T \\ &= \mathbf{F}^e \cdot [\underset{\sim}{\mathbf{C}} : (\mathbf{F}^{eT} \cdot \mathbf{D}^e \cdot \mathbf{F}^e)] \cdot \mathbf{F}^{eT} + \mathbf{D}^e \cdot \boldsymbol{\tau} + \mathbf{W}^e \cdot \boldsymbol{\tau} + \boldsymbol{\tau} \cdot \mathbf{D}^{eT} + \boldsymbol{\tau} \cdot \mathbf{W}^{eT} \\ &= \mathbf{F}^e \cdot [\underset{\sim}{\mathbf{C}} : (\mathbf{F}^{eT} \cdot \mathbf{D}^e \cdot \mathbf{F}^e)] \cdot \mathbf{F}^{eT} + \mathbf{D}^e \cdot \boldsymbol{\tau} + \boldsymbol{\tau} \cdot \mathbf{D}^e + \mathbf{W}^e \cdot \boldsymbol{\tau} - \boldsymbol{\tau} \cdot \mathbf{W}^e. \end{aligned} \tag{C.6}$$

The first term on the right hand side can be rewritten as follows (using indicial notation):

$$\begin{aligned}\left[\mathbf{F}^e\cdot[\underset{\sim}{\mathbf{C}}:(\mathbf{F}^{eT}\cdot\mathbf{D}^e\cdot\mathbf{F}^e)]\cdot\mathbf{F}^{eT}\right]_{ij} &= F^e_{ip}[\underset{\sim}{C}:(\mathbf{F}^{eT}\cdot\mathbf{D}^e\cdot\mathbf{F}^e)]_{pq}F^e_{jq}\\ &= F^e_{ip}\underset{\sim}{C}_{pqrs}(\mathbf{F}^{eT}\cdot\mathbf{D}^e\cdot\mathbf{F}^e)_{rs}F^e_{jq}\\ &= F^e_{ip}\underset{\sim}{C}_{pqrs}F^e_{kr}D^e_{kl}F^e_{ls}F^e_{jq}\\ &= F^e_{ip}F^e_{jq}F^e_{kr}F^e_{ls}\underset{\sim}{C}_{pqrs}D^e_{kl}\\ &= (\underset{\sim}{L}^e_t)_{ijkl}D^e_{kl},\end{aligned} \tag{C.7}$$

where

$$(\underset{\sim}{L}^e_t)_{ijkl} = F^e_{ip}F^e_{jq}F^e_{kr}F^e_{ls}\underset{\sim}{C}_{pqrs}\,. \tag{C.8}$$

The expression in (C.6) can now be written as

$$\dot{\boldsymbol{\tau}} = \underset{\sim}{\mathbf{L}}^e_t:\mathbf{D}^e + \mathbf{D}^e\cdot\boldsymbol{\tau} + \boldsymbol{\tau}\cdot\mathbf{D}^e + \mathbf{W}^e\cdot\boldsymbol{\tau} - \boldsymbol{\tau}\cdot\mathbf{W}^e\,, \tag{C.9}$$

which can be recast to

$$\dot{\boldsymbol{\tau}} - \mathbf{W}^e\cdot\boldsymbol{\tau} + \boldsymbol{\tau}\cdot\mathbf{W}^e = \underset{\sim}{\mathbf{L}}^e_t:\mathbf{D}^e + \mathbf{D}^e\cdot\boldsymbol{\tau} + \boldsymbol{\tau}\cdot\mathbf{D}^e \tag{C.10}$$

or

$$\overset{\triangledown}{\boldsymbol{\tau}}^e = \underset{\sim}{\mathbf{L}}^e_t:\mathbf{D}^e + \mathbf{D}^e\cdot\boldsymbol{\tau} + \boldsymbol{\tau}\cdot\mathbf{D}^e\,, \tag{C.11}$$

where

$$\overset{\triangledown}{\boldsymbol{\tau}}^e = \dot{\boldsymbol{\tau}} - \mathbf{W}^e\cdot\boldsymbol{\tau} + \boldsymbol{\tau}\cdot\mathbf{W}^e\,. \tag{C.12}$$

Eq. (C.11) is expressed equivalently by

$$\overset{\triangledown}{\boldsymbol{\tau}}^e = \underset{\sim}{\mathbf{L}}^e_t:\mathbf{D}^e + \underset{\sim}{\mathbf{T}}:\mathbf{D}^e\,, \tag{C.13}$$

where $\underset{\sim}{\mathbf{T}}$ is expressed in indicial notation as

$$T_{ijkl} = \tfrac{1}{2}(\tau_{ik}\delta_{jl} + \tau_{jl}\delta_{ik} + \tau_{il}\delta_{jk} + \tau_{jk}\delta_{il})\,. \tag{C.14}$$

Eq. (C.13) can now be expressed as

$$\overset{\triangledown}{\boldsymbol{\tau}}^e = \underset{\sim}{\mathbf{L}}^e_t:\mathbf{D}^e + \underset{\sim}{\mathbf{T}}:\mathbf{D}^e = (\underset{\sim}{\mathbf{L}}^e_t + \underset{\sim}{\mathbf{T}}):\mathbf{D}^e = \underset{\sim}{\mathbf{L}}^e:\mathbf{D}^e\,, \tag{C.15}$$

where

$$\underset{\sim}{\mathbf{L}}_e = \underset{\sim}{\mathbf{L}}^t_e + \underset{\sim}{\mathbf{T}}\,. \tag{C.16}$$

Based on the description of the elastic part of the Jaumann rate of the Kirchhoff stress, the total Jaumann rate of the Kirchhoff stress can be written as

$$\begin{aligned}\overset{\nabla}{\boldsymbol{\tau}} &= \dot{\boldsymbol{\tau}} - \mathbf{W}\cdot\boldsymbol{\tau} + \boldsymbol{\tau}\cdot\mathbf{W} = \dot{\boldsymbol{\tau}} - (\mathbf{W}^e + \mathbf{W}^p)\cdot\boldsymbol{\tau} + \boldsymbol{\tau}\cdot(\mathbf{W}^e + \mathbf{W}^p) \\ &= \dot{\boldsymbol{\tau}} - \mathbf{W}^e\cdot\boldsymbol{\tau} - \mathbf{W}^p\cdot\boldsymbol{\tau} + \boldsymbol{\tau}\cdot\mathbf{W}^e - \mathbf{W}^p\cdot\boldsymbol{\tau} + \boldsymbol{\tau}\cdot\mathbf{W}^p \\ &= \overset{\nabla}{\boldsymbol{\tau}}{}^e - \mathbf{W}^p\cdot\boldsymbol{\tau} + \boldsymbol{\tau}\cdot\mathbf{W}^p.\end{aligned} \tag{C.17}$$

Substituting Eqs. (31) and (C.15) into Eq. (C.17) gives

$$\begin{aligned}\overset{\nabla}{\boldsymbol{\tau}} &= \underset{\sim}{\mathbf{L}}^e : \mathbf{D}^e - \sum_\delta \dot{\gamma}^\delta(\mathbf{Q}^\delta\cdot\boldsymbol{\tau} - \boldsymbol{\tau}\cdot\mathbf{Q}^\delta) \\ &= \underset{\sim}{\mathbf{L}}^e : (\mathbf{D} - \mathbf{D}^p - \mathbf{D}^h) - \sum_\delta \dot{\gamma}^\delta(\mathbf{Q}^\delta\cdot\boldsymbol{\tau} - \boldsymbol{\tau}\cdot\mathbf{Q}^\delta) \\ &= \underset{\sim}{\mathbf{L}}^e : \mathbf{D} - \underset{\sim}{\mathbf{L}}^e : \left(\sum_\delta \dot{\gamma}^\delta \mathbf{P}^\delta\right) - \underset{\sim}{\mathbf{L}}^e : \mathbf{D}^h - \sum_\delta \dot{\gamma}^\delta(\mathbf{Q}^\delta\cdot\boldsymbol{\tau} - \boldsymbol{\tau}\cdot\mathbf{Q}^\delta) \\ &= \underset{\sim}{\mathbf{L}}^e : \mathbf{D} - \underset{\sim}{\mathbf{L}}^e : \mathbf{D}^h - \sum_\delta \dot{\gamma}^\alpha\left[\underset{\sim}{\mathbf{L}}^e : \mathbf{P}^\delta + \mathbf{Q}^\delta\cdot\boldsymbol{\tau} - \boldsymbol{\tau}\cdot\mathbf{Q}^\delta\right] \\ &= \underset{\sim}{\mathbf{L}}^e : \mathbf{D} - \underset{\sim}{\mathbf{L}}^e : \mathbf{D}^h - \sum_\delta \dot{\gamma}^\delta \boldsymbol{\Phi}^\delta,\end{aligned} \tag{C.18}$$

where

$$\boldsymbol{\Phi}^\delta = \underset{\sim}{\mathbf{L}}^e : \mathbf{P}^\delta + \mathbf{Q}^\delta\cdot\boldsymbol{\tau} - \boldsymbol{\tau}\cdot\mathbf{Q}^\delta. \tag{C.19}$$

To conclude the derivation, it is necessary to express the slip rate $\dot{\gamma}^\delta$ in terms of $\mathbf{D}$. This can be done through the use of the consistency condition:

$$\dot{f}^\delta = \dot{\tau}^\delta - \dot{\tau}^\delta_{cr} = 0. \tag{C.20}$$

The derivative of the resolved shear stress is evaluated directly from Eq. (58):

$$\dot{\tau}^\delta = \dot{\mathbf{m}}^\delta\cdot\boldsymbol{\tau}\cdot\mathbf{s}^\delta + \mathbf{m}^\delta\cdot\dot{\boldsymbol{\tau}}\cdot\mathbf{s}^\delta + \mathbf{m}^\delta\cdot\boldsymbol{\tau}\cdot\dot{\mathbf{s}}^\delta. \tag{C.21}$$

The rate of change of $\mathbf{s}^\delta$ and $\mathbf{m}^\delta$ can be determined using Eqs. (22) and (25), and taking into account that since $\mathbf{s}_0^\delta$ and $\mathbf{m}_0^\delta$ are fixed in time, $\dot{\mathbf{s}}_0^\delta$ and $\dot{\mathbf{m}}_0^\delta$ both vanish:

$$\begin{aligned}\dot{\mathbf{s}}^\delta &= \tfrac{d}{dt}\left(\mathbf{F}^e\cdot\mathbf{s}_0^\delta\right) = \dot{\mathbf{F}}^e\cdot\mathbf{s}_0^\delta + \mathbf{F}^e\cdot\dot{\mathbf{s}}_0^\delta = \dot{\mathbf{F}}^e\cdot\mathbf{s}_0^\delta \\ &= \left(\mathbf{L}^e\cdot\mathbf{F}^e\right)\cdot\mathbf{s}_0^\delta = \mathbf{L}^e\cdot\left(\mathbf{F}^e\cdot\mathbf{s}_0^\delta\right) \\ &= \mathbf{L}^e\cdot\mathbf{s}^\delta\end{aligned} \tag{C.22}$$

and

$$\begin{aligned}&\dot{\mathbf{m}}_0^\delta = \tfrac{d}{dt}\left(\mathbf{m}^\delta\cdot\mathbf{F}^e\right) = \dot{\mathbf{m}}^\delta\cdot\mathbf{F}^e + \mathbf{m}^\delta\cdot\dot{\mathbf{F}}^e = 0 \\ &\Rightarrow \dot{\mathbf{m}}^\delta\cdot\mathbf{F}^e = -\mathbf{m}^\delta\cdot\dot{\mathbf{F}}^e \Rightarrow \dot{\mathbf{m}}^\delta = -\mathbf{m}^\delta\cdot\dot{\mathbf{F}}^e\cdot\mathbf{F}^{e-1} \\ &\Rightarrow \dot{\mathbf{m}}^\delta = -\mathbf{m}^\delta\cdot\mathbf{L}^e.\end{aligned} \tag{C.23}$$

The substitution of Eqs. (C.22) and (C.23) into (C.21) yields

$$
\begin{aligned}
\dot{\tau}^{\delta} &= -\mathbf{m}^{\delta}\cdot\mathbf{L}^{e}\cdot\boldsymbol{\tau}\cdot\mathbf{s}^{\delta}+\mathbf{m}^{\delta}\cdot\dot{\boldsymbol{\tau}}\cdot\mathbf{s}^{\delta}+\mathbf{m}^{\delta}\cdot\boldsymbol{\tau}\cdot\mathbf{L}^{e}\cdot\mathbf{s}^{\delta}\\
&= \mathbf{m}^{\delta}\cdot(\dot{\boldsymbol{\tau}}-\mathbf{L}^{e}\cdot\boldsymbol{\tau}+\boldsymbol{\tau}\cdot\mathbf{L}^{e})\cdot\mathbf{s}^{\delta}\\
&= \mathbf{m}^{\delta}\cdot\left(\dot{\boldsymbol{\tau}}-(\mathbf{D}^{e}+\mathbf{W}^{e})\cdot\boldsymbol{\tau}+\boldsymbol{\tau}\cdot(\mathbf{D}^{e}+\mathbf{W}^{e})\right)\cdot\mathbf{s}^{\delta}\\
&= \mathbf{m}^{\delta}\cdot\left(\dot{\boldsymbol{\tau}}-\mathbf{W}^{e}\cdot\boldsymbol{\tau}+\boldsymbol{\tau}\cdot\mathbf{W}^{e}-\mathbf{D}^{e}\cdot\boldsymbol{\tau}+\boldsymbol{\tau}\cdot\mathbf{D}^{e}\right)\cdot\mathbf{s}^{\delta}\\
&= \mathbf{m}^{\delta}\cdot\left(\overset{\nabla}{\boldsymbol{\tau}}{}^{e}-\mathbf{D}^{e}\cdot\boldsymbol{\tau}+\boldsymbol{\tau}\cdot\mathbf{D}^{e}\right)\cdot\mathbf{s}^{\delta}\\
&= \mathbf{m}^{\delta}\cdot\overset{\nabla}{\boldsymbol{\tau}}{}^{e}\cdot\mathbf{s}^{\delta}+\mathbf{m}^{\delta}\cdot\left(\boldsymbol{\tau}\cdot\mathbf{D}^{e}-\mathbf{D}^{e}\cdot\boldsymbol{\tau}\right)\cdot\mathbf{s}^{\delta}.
\end{aligned}
\tag{C.24}
$$

The first term on the right side can be written as

$$
\begin{aligned}
\mathbf{m}^{\delta}\cdot\overset{\nabla}{\boldsymbol{\tau}}{}^{e}\cdot\mathbf{s}^{\delta} &= m_i^{\delta}\,\overset{\nabla}{\tau}{}^{e}_{ij}\,s_j^{\delta}=(m_i^{\delta}s_j^{\delta})\,\overset{\nabla}{\tau}{}^{e}_{ij}\\
&= \mathbf{m}^{\delta}\mathbf{s}^{\delta}:\overset{\nabla}{\boldsymbol{\tau}}{}^{e}=sym(\mathbf{m}^{\delta}\mathbf{s}^{\delta}):\overset{\nabla}{\boldsymbol{\tau}}{}^{e}\\
&= \mathbf{P}^{\delta}:\overset{\nabla}{\boldsymbol{\tau}}{}^{e}=\mathbf{P}^{\delta}:(\underset{\sim}{\mathbf{L}}{}^{e}:\mathbf{D}^{e}),
\end{aligned}
\tag{C.25}
$$

and the second term can be written as

$$
\begin{aligned}
\mathbf{m}^{\delta}\cdot\left(\boldsymbol{\tau}\cdot\mathbf{D}^{e}-\mathbf{D}^{e}\cdot\boldsymbol{\tau}\right)\cdot\mathbf{s}^{\delta} &= \mathbf{m}^{\delta}\cdot\boldsymbol{\tau}\cdot\mathbf{D}^{e}\cdot\mathbf{s}^{\delta}-\mathbf{m}^{\delta}\cdot\mathbf{D}^{e}\cdot\boldsymbol{\tau}\cdot\mathbf{s}^{\delta}\\
&= m_i^{\delta}\tau_{ik}D^{e}_{kj}s_j^{\delta}-m_k^{\delta}D^{e}_{kj}\tau_{ji}s_i^{\delta}\\
&= m_i^{\delta}\tau_{ik}s_j^{\delta}D^{e}_{kj}-m_k^{\delta}\tau_{ji}s_i^{\delta}D^{e}_{kj}\\
&= (m_i^{\delta}\tau_{ik}s_j^{\delta}-m_k^{\delta}\tau_{ji}s_i^{\delta})D^{e}_{kj}\\
&= (\mathbf{m}^{\delta}\cdot\boldsymbol{\tau}\mathbf{s}^{\delta}-\mathbf{m}^{\delta}\,\boldsymbol{\tau}\cdot\mathbf{s}^{\delta}):\mathbf{D}^{e}\\
&= sym(\mathbf{m}^{\delta}\cdot\boldsymbol{\tau}\mathbf{s}^{\delta}-\mathbf{m}^{\delta}\,\boldsymbol{\tau}\cdot\mathbf{s}^{\delta}):\mathbf{D}^{e}\\
&= \tfrac{1}{2}(\boldsymbol{\tau}\cdot\mathbf{m}^{\delta}\,\mathbf{s}^{\delta}+\mathbf{s}^{\delta}\mathbf{m}^{\delta}\cdot\boldsymbol{\tau}-\mathbf{m}^{\delta}\mathbf{s}^{\delta}\cdot\boldsymbol{\tau}-\boldsymbol{\tau}\cdot\mathbf{s}^{\delta}\mathbf{m}^{\delta}):\mathbf{D}^{e}\\
&= \left[\boldsymbol{\tau}\cdot\tfrac{1}{2}(\mathbf{m}^{\delta}\,\mathbf{s}^{\delta}-\mathbf{s}^{\delta}\mathbf{m}^{\delta})+\tfrac{1}{2}(\mathbf{s}^{\delta}\mathbf{m}^{\delta}-\mathbf{m}^{\delta}\,\mathbf{s}^{\delta})\cdot\boldsymbol{\tau}\right]:\mathbf{D}^{e}\\
&= [\mathbf{Q}^{\delta}\cdot\boldsymbol{\tau}-\boldsymbol{\tau}\cdot\mathbf{Q}^{\delta}]:\mathbf{D}^{e}.
\end{aligned}
\tag{C.26}
$$

Substituting Eqs. (C.25) and (C.26) into Eq. (C.24) yields

$$
\begin{aligned}
\dot{\tau}^{\delta} &= \mathbf{m}^{\delta}\cdot\overset{\nabla}{\boldsymbol{\tau}}{}^{e}\cdot\mathbf{s}^{\delta}+\mathbf{m}^{\delta}\cdot\left(\boldsymbol{\tau}\cdot\mathbf{D}^{e}-\mathbf{D}^{e}\cdot\boldsymbol{\tau}\right)\cdot\mathbf{s}^{\delta}\\
&= \mathbf{P}^{\delta}:\underset{\sim}{\mathbf{L}}{}^{e}:\mathbf{D}^{e}+[\mathbf{Q}^{\delta}\cdot\boldsymbol{\tau}-\boldsymbol{\tau}\cdot\mathbf{Q}^{\delta}]:\mathbf{D}^{e}\\
&= \left[\mathbf{P}^{\delta}:\underset{\sim}{\mathbf{L}}{}^{e}+\mathbf{Q}^{\delta}\cdot\boldsymbol{\tau}-\boldsymbol{\tau}\cdot\mathbf{Q}^{\delta}\right]:\mathbf{D}^{e}\\
&= \boldsymbol{\Phi}^{\delta}:\mathbf{D}^{e}=\boldsymbol{\Phi}^{\delta}:(\mathbf{D}-\mathbf{D}^{p})\\
&= \boldsymbol{\Phi}^{\delta}:\mathbf{D}-\boldsymbol{\Phi}^{\delta}:\sum_{\beta}\dot{\gamma}^{\beta}\mathbf{P}^{\beta},
\end{aligned}
\tag{C.27}
$$

where

$$\boldsymbol{\Phi}^{\delta} = \mathbf{P}^{\delta} : \underset{\sim}{\mathbf{L}}^{e} + \mathbf{Q}^{\delta} \cdot \boldsymbol{\tau} - \boldsymbol{\tau} \cdot \mathbf{Q}^{\delta} . \tag{C.28}$$

Substituting Eqs. (1) and (C.28) into Eq. (C.20) gives

$$\begin{aligned} &\dot{\tau}^{\delta} - \dot{\tau}_{cr}^{\delta} = \boldsymbol{\Phi}^{\delta} : \mathbf{D} - \boldsymbol{\Phi}^{\delta} : \sum_{\beta} \dot{\gamma}^{\beta} \mathbf{P}^{\beta} - \sum_{\beta} h_{\delta\beta} \dot{\gamma}^{\beta} = 0 \\ &\Rightarrow \boldsymbol{\Phi}^{\delta} : \mathbf{D} - \sum_{\beta} \dot{\gamma}^{\beta} (\boldsymbol{\Phi}^{\delta} : \mathbf{P}^{\beta}) - \sum_{\beta} h_{\delta\beta} \dot{\gamma}^{\beta} = 0 \\ &\Rightarrow \sum_{\beta} \dot{\gamma}^{\beta} (h_{\delta\beta} + \boldsymbol{\Phi}^{\delta} : \mathbf{P}^{\beta}) = \boldsymbol{\Phi}^{\alpha} : \mathbf{D} \\ &\Rightarrow \sum_{\beta} A^{\delta\beta} \dot{\gamma}^{\beta} = \boldsymbol{\Phi}^{\delta} : \mathbf{D}, \end{aligned} \tag{C.29}$$

where

$$A^{\delta\beta} = h_{\delta\beta} + \boldsymbol{\Phi}^{\delta} : \mathbf{P}^{\beta} . \tag{C.30}$$

Letting $B^{\delta\beta}$ be the inverse of $A^{\delta\beta}$, the shear strain can be written as

$$\dot{\gamma}^{\delta} = \sum_{\beta} B^{\delta\beta} \boldsymbol{\Phi}^{\beta} : \mathbf{D} . \tag{C.31}$$

Defining

$$\boldsymbol{\Psi}^{\delta} = \sum_{\beta} B^{\delta\beta} \boldsymbol{\Phi}^{\beta} , \tag{C.32}$$

Eq. (C.18) can now be written as

$$\begin{aligned} \overset{\triangledown}{\boldsymbol{\tau}} &= \underset{\sim}{\mathbf{L}}^{e} : \mathbf{D} - \sum_{\delta} \boldsymbol{\Phi}^{\delta} (\boldsymbol{\Psi}^{\delta} : \mathbf{D}) \\ &= \underset{\sim}{\mathbf{L}}^{e} : \mathbf{D} - \left(\sum_{\delta} \boldsymbol{\Phi}^{\delta} \boldsymbol{\Psi}^{\delta} \right) : \mathbf{D} \\ &= \left(\underset{\sim}{\mathbf{L}}^{e} - \sum_{\delta} \boldsymbol{\Phi}^{\delta} \boldsymbol{\Psi}^{\delta} \right) : \mathbf{D}. \end{aligned} \tag{C.33}$$

Finally, by comparing the form of Eqs. (C.2) and (C.33), it can be seen that the approximation to the tangent modulus is written as

$$\underset{\sim}{\mathbf{L}}_{J} = \underset{\sim}{\mathbf{L}}^{e} - \sum_{\delta} \boldsymbol{\Phi}^{\delta} \boldsymbol{\Psi}^{\delta} . \tag{C.34}$$

Appendix D: Analytical Solution to the Hardening Evolution for a Single Active Slip System

The hardening evolution given in Eq. (63) can be solved analytically to be compared to the case of a single active slip system. The hardening evolution can be restated as

$$\frac{d\tau_{cr}}{d\gamma} = H - R\left(\tau_{cr} - \tau_0\right). \tag{D.1}$$

The superscript α is dropped while considering the case in which only one slip system is active. This equation can be solved for τ_{cr} using separation of variables as follows:

$$\begin{aligned}
&\frac{d\tau_{cr}}{H - R\left(\tau_{cr} - \tau_0\right)} = d\gamma \\
&\Rightarrow -\frac{1}{R}\ln\left[H - R\left(\tau_{cr} - \tau_0\right)\right] = \gamma + C_1 \\
&\Rightarrow \ln\left[H - R\left(\tau_{cr} - \tau_0\right)\right] = -R\gamma + C_2 \\
&\Rightarrow H - R\left(\tau_{cr} - \tau_0\right) = \exp(-R\gamma + C_2) \\
&\Rightarrow -R\tau_{cr} = C_3\exp(-R\gamma) - H - R\tau_0 \\
&\Rightarrow \tau_{cr} = C_4\exp(-R\gamma) + \frac{H}{R} + \tau_0.
\end{aligned} \tag{D.2}$$

The unknown constant can be determined from the condition that for no plastic shear strain ($\gamma = 0$), the critical resolved shear stress is given by $\tau_{cr}(\gamma = 0) = \tau_0$. The solution for τ_{cr} can then be expressed as

$$\tau_{cr} = -\frac{H}{R}\exp(-R\gamma) + \frac{H}{R} + \tau_0. \tag{D.3}$$

This equation is plotted in Fig. 3 for the case $\tau_0 = 20$ MPa, $H = 125$ MPa, and $R = 4$.